Collective Behavior of Asperities Before Large Stick-Slip Events

Weiwei Shu, Olivier Lengliné, Jean Schmittbuhl

JGR Solid Earth

RESEARCH ARTICLE
10.1029/2023JB026696

Collective Behavior of Asperities Before Large Stick-Slip Events

Weiwei Shu[1], **Olivier Lengliné**[1], **and Jean Schmittbuhl**[1]

[1]Université de Strasbourg, CNRS, ITES UMR 7063, Strasbourg, France

Key Points:

- We propose a novel direct-shear setup to observe the collective behavior of asperities along an analog fault interface during stick-slips
- Scaling laws, that mimic those of slow slip events, are observed in our experiments and originate during the slip-strengthening phase
- Large scale quenched topography of the asperities along the interface has a direct impact on the interseismic coupling

Supporting Information:

Supporting Information may be found in the online version of this article.

Correspondence to:

W. Shu,
w.shu@unistra.fr

Citation:

Shu, W., Lengliné, O., & Schmittbuhl, J. (2023). Collective behavior of asperities before large stick-slip events. *Journal of Geophysical Research: Solid Earth*, *128*, e2023JB026696. https://doi.org/10.1029/2023JB026696

Received 9 MAR 2023
Accepted 29 AUG 2023

Author Contributions:

Conceptualization: Weiwei Shu, Olivier Lengliné, Jean Schmittbuhl
Data curation: Weiwei Shu
Funding acquisition: Jean Schmittbuhl
Investigation: Weiwei Shu, Olivier Lengliné
Project Administration: Jean Schmittbuhl
Software: Weiwei Shu, Olivier Lengliné
Supervision: Olivier Lengliné, Jean Schmittbuhl
Validation: Weiwei Shu, Olivier Lengliné
Visualization: Weiwei Shu
Writing – original draft: Weiwei Shu

Abstract The multi-scale roughness of a fault interface is responsible for multiple asperities that establish a complex and discrete set of real contacts. Since asperities control the initiation and evolution of the fault slip, it is important to explore the intrinsic relationships between the collective behavior of local asperities and the frictional stability of the global fault. Here we propose a novel analog experimental approach, which allows us to capture the temporal evolution of the slip of each asperity on a faulting interface. We find that many destabilizing events at the local asperity scale occurred in the slip-strengthening stage which is conventionally considered as the stable regime of a fault. We compute the interseismic coupling to evaluate the slipping behaviors of asperities during the slip-strengthening stage. We evidence that the interseismic coupling can be affected by the elastic interactions between asperities through the embedding soft matrix. Scaling laws of natural slow slip events are reproduced by our setup in particular the moment-duration scaling. We also evidence an unexpected persistency of a disordering of the asperities through the seismic cycles despite the relaxation effects of the large slip events.

Plain Language Summary Earthquakes are the results of a slip along a rough fault on which a complex and discrete set of asperities establish the interfacial contacts and control the frictional stability of the fault. We propose a novel experimental setup capable of measuring directly the subtle motion of individual asperities on an analog faulting interface. By capturing the temporal evolution of the slip of each asperity, we link the mechanical behavior of the global fault with the collective behavior of local asperities. Many destabilizing events at the local asperity scale are found during the globally stable stage of the fault. We prove that the interseismic coupling of asperities is affected by the normal load, the peak height of asperities, and the interactions between asperities. The spatiotemporal interactions of asperities are quantified as slip episodes to mimic the ruptures including both stable and unstable slips. With the catalog of slip episodes, we reproduce the significant characteristics and scaling laws observed in natural faults, such as the magnitude-frequency distribution and the moment-duration scaling. Such upscaling suggests that our results can be extrapolated to natural faults and provide insights into fault physics and mechanics.

1. Introduction

Crustal fault interfaces display geological heterogeneities at various scales (Ben-Zion & Sammis, 2003; Chester et al., 1993; Faulkner et al., 2003). In particular, exhumed fault surfaces exhibit a complex topography characterized by height variations at all scales (Candela et al., 2009, 2012; Power et al., 1987; Schmittbuhl et al., 1993, 1995; Scholz, 2019). Supposing that the roughness of these interfaces is similar to those of active faults at depth, it implies that the frictional interface is formed by a complex set of junctions across the two opposite surfaces in contact (Pohrt & Popov, 2012; Schmittbuhl et al., 2006). These junctions are commonly known as asperities (Bhushan, 1998). They have been characterized at the laboratory scale as microcontacts (Dieterich & Kilgore, 1994) where the resistance to an imposed shear stress is shown to be governed by the initiation and evolution of the fault slip (Scholz, 2019).

The presence of these asperities on the fault is supported by the observation of small repeating earthquakes, supposedly representing cohesive zones that fail periodically under constant loading (Frank, 2016; Nadeau & Johnson, 1998). The role of such asperities in the behavior of earthquakes has long been recognized. For example, it is suggested that small and scattered asperities on a subduction interface may lead only to a minor release of the seismic moment (Ruff & Kanamori, 1983). On the other hand, a great earthquake may involve the simultaneous rupture of multiple asperities, such as the 1960 M_W 9.5 Chile earthquake (Moreno et al., 2009) or the 2004 M_W 9.2 Sumatra-Andaman earthquake (Subarya et al., 2006). Such examples have been interpreted in a framework

Writing – review & editing: Weiwei Shu, Olivier Lengliné, Jean Schmittbuhl

drawing a strong link between the rupture synchronization of asperities and the magnitude of the impending earthquake (Lay et al., 1982; Lay & Kanamori, 1981). The role of asperities on the behavior of the faulting interface is not limited to dynamic rupture events. Indeed, the interseismic phase is also strongly impacted by the presence of such strong contact areas. This notably arises as locked patches can create stress shadows which lead to reduced interseismic slip rates on the surroundings of the asperity (Bürgmann et al., 2005) and thus a spatial modulation of the interseismic coupling (Perfettini et al., 2010).

Numerical models have addressed the behavior of a fault interface comprising multiple asperities. A number of simulations represent the interface notably in the context of the rate-and-state friction framework (Dieterich, 1979; Marone, 1998; Ruina, 1983) and asperities are presented as distinct patches spatially distributed over the fault plane with distinct frictional parameters (Ariyoshi et al., 2009; Dublanchet et al., 2013; Li & Rubin, 2017; Luo & Ampuero, 2018). In these numerical models, the asperities are usually considered as velocity-weakening patches and are therefore defined to be potentially unstable. These models indicate that the mechanical response of a fault is evidently affected by the interactions of discrete asperities surrounded by aseismic creep areas. For instance, a variable density of asperities (Dublanchet et al., 2013), which is the ratio between the total area covered by asperities and the total area of the fault plane is proposed and utilized to explain at which condition the fault will be ruptured entirely or locally. Incorporating roughness on the fault plane (as fluctuations of the normal stress), Cattania and Segall (2021) show that this heterogeneity modulates the slip stability across the fault. Finally, Romanet et al. (2018) demonstrate that the sliding diversity of a fault can be obtained from geometrical complexities alone, without the need for the complexity of the friction law. All these numerical approaches, therefore, point to the importance of these asperities and their interactions in controlling fault mechanics. However, these models are severely limited by the computational cost of simulating heterogeneities with a variable size over a large time and space domain and inherently only describe a limited aspect of the ongoing physics.

At the laboratory scale, numerous experiments on rock samples have also shown that fault roughness plays a crucial role in fault slip behavior (Goebel et al., 2017; Harbord et al., 2017; Morad et al., 2022; Xu et al., 2023; Yamashita et al., 2021) as it controls actual stress conditions at contacting asperities (Aubry et al., 2020). These results imply that the stress heterogeneity at local asperities is significant for influencing fault slip behavior. However, these experiments usually analyze the effects of asperities by comparing the initial and final roughness of the fault interface as the nontransparent rock slabs cannot provide the possibility to capture what is happening on the interface during the fault slip process. On the contrary, some other experiments take advantage of the transparency of analog materials (e.g., Poly-methyl-methacrylate, PMMA) to optically observe the asperities distributed on the interface (Jestin et al., 2019; Lengliné et al., 2012; Selvadurai & Glaser, 2015, 2017), which provides a possibility for the direct monitoring of the faulting interface. Although the contacts were captured during these experiments, it was not possible to track the slip at each point during shearing.

Here we present a novel experimental setup that aims at capturing the slip as a function of time for each asperity on a sheared interface. Our experimental setup is much simpler than a complex fault zone system, which has no mineralogy, no fluid, and no chemical transformation, but the fundamental process of interest, the relationship between the collective behavior of local asperities and the stability regime of the global fault system, remains similar. Specifically, this novel experimental approach allows a thick transparent PMMA plate to slide slowly on a customized surface with height variations, on which asperities are modeled by numerous identical spherical PMMA beads embedded in a softer polymer base. Thanks to a high-resolution camera, our setup is capable of measuring directly the subtle motion of local asperities on the interface during the whole slipping process, which helps to understand the time-and-space dependent behavior of each single asperity. The mechanical response of the global fault system is well recorded and explained through the collective behavior of local asperities. The link between the fault topography and the interseismic coupling is also investigated. In addition, the spatio-temporal interactions of asperities are quantified as collective slip episodes mimicking fault ruptures including both stable and unstable slips. To give some geophysical implications, the effective upscaling from the analog interface to natural faults is demonstrated by reproducing significant characteristics and scaling-laws observed in natural fault systems.

2. Experimental Setup

We build an analog model of a shear interface that aims at reproducing the typical mechanical structure of a natural fault core. We consider that a fault zone consists of several key elements. At the interface, the roughness of the

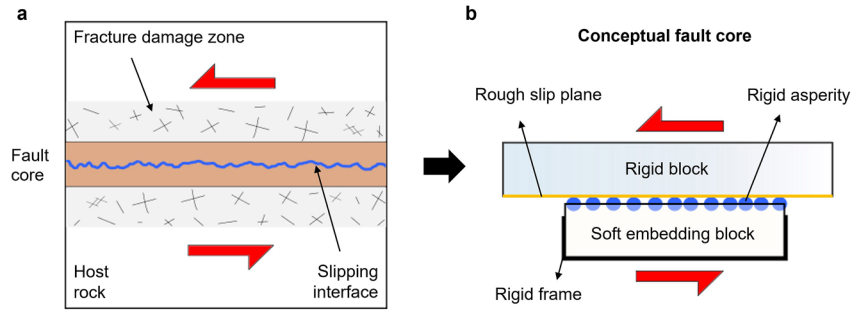

Figure 1. (a) Sketch of a typical natural fault zone showing a rough frictional slipping interface subjected to shear. (b) Conceptual model of the analog shear interface derived from the natural fault core structure. The rigid asperities embedded in the soft thick block establish a rough slip plane beneath the top rigid block.

fault topography creates contacts on a number of discrete sites, that is, asperities, that are here modeled as PMMA beads. The core of the fault, which consists generally in a heavily fractured medium (Chester & Chester, 1998; Schulz & Evans, 2000) is represented in our setup with a soft material surrounding the PMMA beads. At a greater distance from the fault, the number of damage decreases (Ben-Zion & Sammis, 2003; Mitchell & Faulkner, 2009; Stierman, 1984), and the fault becomes stiffer which translates in our setup in a rigid base attached to the soft material (Figure 1). The asperities are in contact with a top rigid block and establish a rough slip plane, while the soft embedding block fixed within the bottom rigid frame is easily deformed. This thick, rough, and deformable interface allows us to study the interactions of asperities and their collective behavior with respect to the frictional stability of the fault interface.

2.1. Sample Preparation and Characterization

To prepare such a model of multi-asperity contact, numerous identical spherical PMMA beads (a total number of 175) with a radius R of 3 mm are embedded in a soft block. The soft block is composed of silicone (BLUESIL RTV 3428 A&B product from the Elkem Company), with dimensions $10 \times 10 \times 3.0$ cm. The preparation of the sample consists in first pouring a thin layer (of the thickness of a bead radius) of edible gelatin mixed with water at the bottom of a mold. Then PMMA beads are dropped randomly in this layer all over the interface. After the gelatin layer solidifies, we then pour the liquid silicon into the mold to cover the beads and wait for at least 24 hr at room temperature for its solidification. Finally, we take out the upside-down sample and remove the mixture of gelatin and water. Following the procedures above, we customize an experimental sample where multiple frictional asperities are embedded in the viscoelastic silicone block. Such an experimental design is supported by growing geological evidence suggesting that a mixture of frictional and viscous deformation is responsible for the emerging diversity of fault slip behaviors (Behr & Bürgmann, 2021; Kirkpatrick et al., 2021). The resulting sample is made such that all beads have nearly the same height while being scattered randomly over the sample and its picture is displayed in Figure 2. Physical characteristics of the silicone are derived from the technical datasheet, the relation of Gent (1958) for converting durometer values to Young's modulus, and laboratory measurements of the P-wave velocity of the material. We obtain a P-wave velocity for this material of 1,000 m/s, an S-wave velocity of 19 m/s, a Young's modulus of 1.1 MPa, and a density of 1,100 kg/m^3. The viscoelasticity of the silicone block is also measured and quantified (Figure S1 in Supporting Information S1).

In order to precisely describe the so-formed interface and get the summit heights of all the beads, we measure a high-resolution topographical map for the interface. The data are acquired by a digital microscope profiler (RH-2000, HIROX) and a non-contact Nano Point Scanner (NPS, HIROX). The system uses a white light confocal LED beam with grids of 28 and 100 μm in the x- and y-directions, respectively. The topographical map of the interface is shown in Figure 3a, where the blueish part indicates the embedding silicone block while the discrete circles represent the asperities with different heights. We determine the peak heights of all the asperities (Figure 3b) and statistically analyze their distribution (Figure 3c). The peak heights of asperities (relative to the average silicone upper face level) range from 1.31 to 3.15 mm, with most of them within the peak height interval [1.4, 2.6]. The average peak height is 2.02 mm and the standard deviation of the peak heights is 0.39 mm, which indicates a small variance in the peak heights of asperities. We notice that there is a large-scale trend across the

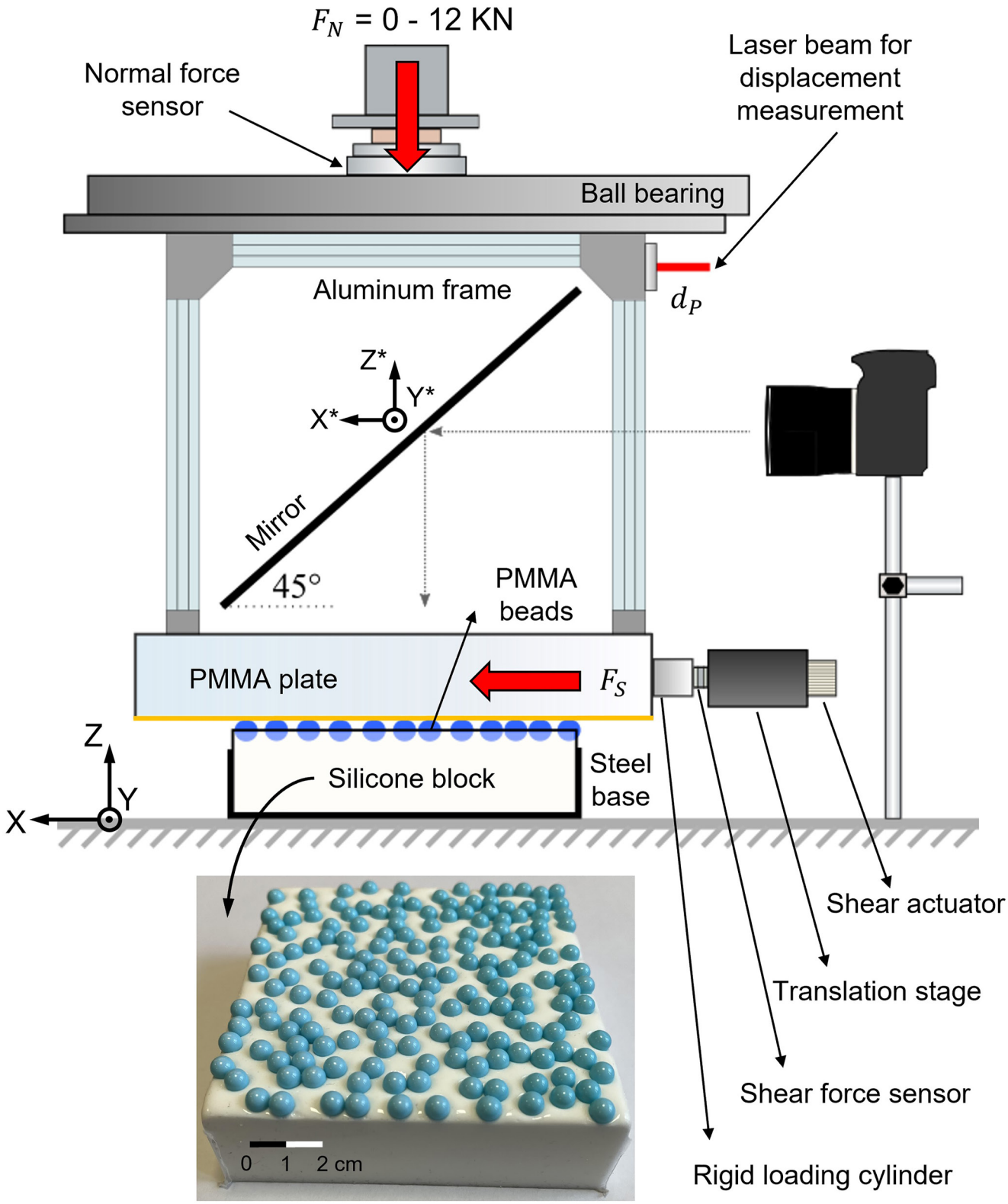

Figure 2. Schematic diagram of the technical experimental setup (side view). The normal force, F_N, and shear force, F_S, are measured by their corresponding sensors. A laser is employed to measure the displacement of the PMMA plate, d_P. A high-resolution camera is utilized with a mirror to monitor the positions of the PMMA beads during the whole shear process. Two axis systems, one attached to the ground and another one attached to the mirror, are represented. The yellow line indicates a rough slip plane established between the PMMA plate and the PMMA beads. The inset shows an image of the PMMA beads embedded in the soft silicone block.

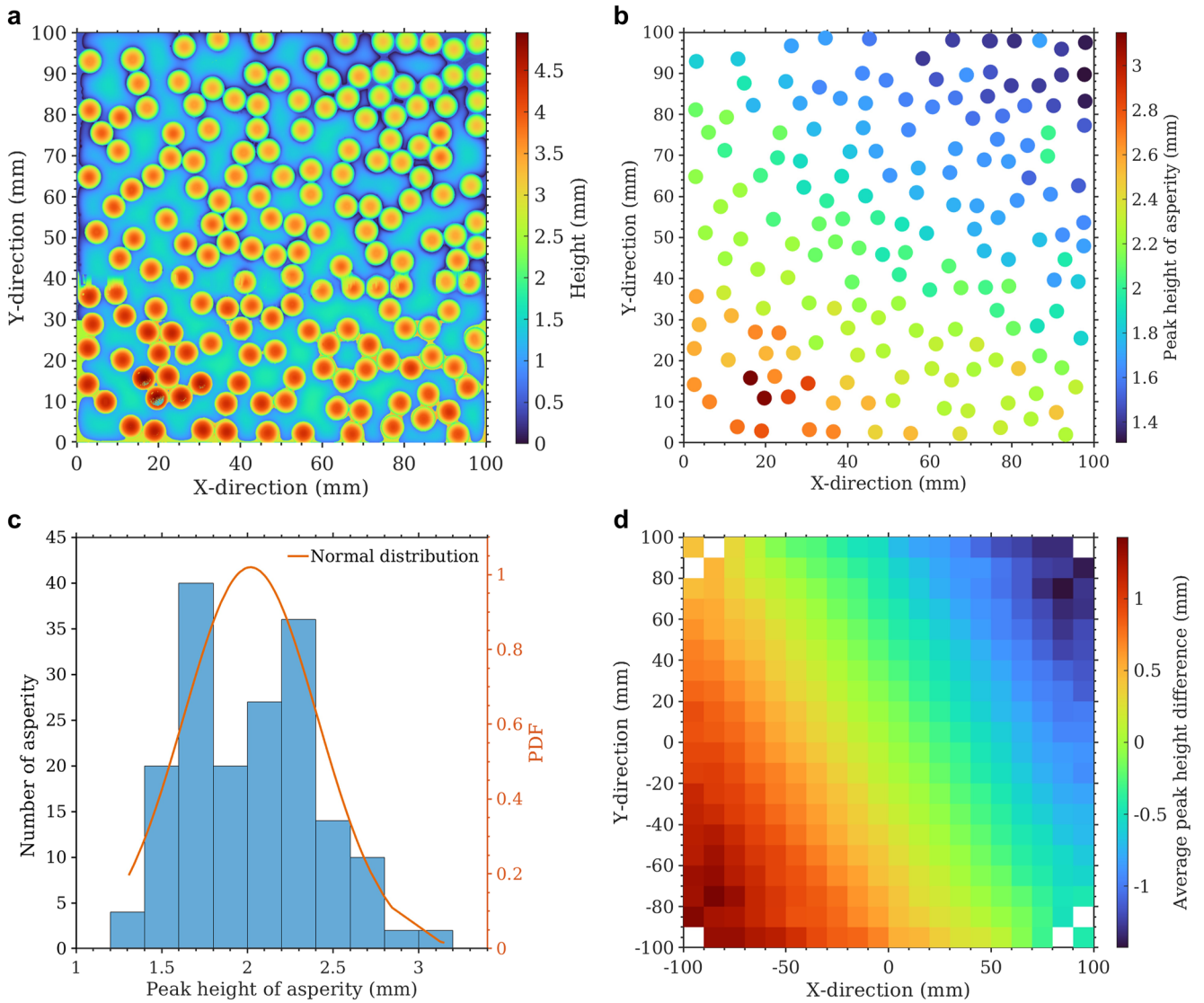

Figure 3. (a) Topographical map of the analog fault interface. The blueish part is the embedding silicone block while the colored circles are the asperities created by the PMMA beads. There are a few non-measured points in the bottom-left corner that have little effect on characterizing the interface. (b) Peak height of each asperity. The minimum and the maximum are 1.31 and 3.15 mm, respectively. (c) Distribution of the peak heights of all the asperities. The asperities with peak heights ranging from 1.4 to 2.6 mm account for the majority. A standard deviation of 0.39 mm indicates a small variance in the peak heights. (d) Average peak height difference as a function of the *x* and *y* direction. This highlights the large scale variation of the peak heights.

entire sample of this peak bead height. This is most likely due to the non-perfect planarity of the gelatin layer. Removing this large-scale trend, we observe that the height difference between neighboring asperities is low. In addition, we compute the average peak height difference between two asperities as a function of the distance in *x* and *y* direction (Figure 3d). We find a pattern highlighting the large scale variation of the peak height but no other correlation of the peak heights emerges.

2.2. Mechanical Loading

To simulate a large-scale, far-field, loading imposed on a fault, the shear of the whole analog interface system is induced by imposing a small displacement rate to the PMMA plate under well-controlled normal loads (Figure 2). Multiple normal loads ranging from 10 to 1,000 N and three displacement rates ranging from 5.0 μm/s to 15.0 μm/s are imposed in the experiments (Table S1 in Supporting Information S1). We consider a simple Hertz model consisting of the serial assembly of the PMMA beads and the silicone block both modeled as elastic

materials (K. Johnson, 1987). As the displacement is imposed on the PMMA beads, the contact area increases and both the PMMA beads and the silicone are deforming. The typical normal stress on the PMMA beads is around 60 MPa, while the typical radius of contact is 200 μm.

PMMA has been widely used, as an analog material, to simulate numerous mechanical processes taking place within the Earth. In particular, frictional processes taking place on natural faults have been investigated using this material, such as fault creep and nucleation phases (e.g., McLaskey et al., 2012; McLaskey & Glaser, 2011; Selvadurai & Glaser, 2015) but also ruptures (e.g., Ben-David et al., 2010; Gvirtzman & Fineberg, 2021; Schmittbuhl & Måløy, 1997). Due to its transparency, the PMMA enables a clear direct observation of the deforming medium (Jestin et al., 2019; Lengliné et al., 2012). The shear modulus of the PMMA is estimated as 2277.1 MPa (Selvadurai & Glaser, 2015).

The normal force F_N is applied by the vertical movement of the rigid load platen driven by a high-precision micro stepper motor (LoadTrac II), and uniformly transferred to the PMMA plate through the ball bearing and the rigid aluminum frame. A sensor of resolution 0.01 N is utilized to record the normal force and maintain a constant normal load throughout the whole duration of an experiment. We run the shear actuator, a combination of servo and stepper motor, with a constant displacement rate V_S to drive the translation stage and the rigid loading cylinder to impose the shear force F_S while maintaining a normal force F_N on the PMMA plate. The loading cylinder is composed of the aluminum alloy 2017A, with a stiffness of 78 N/μm. The shear force F_S is measured using a sensor placed between the cylinder and the translation stage, with a resolution of 0.01 N. The stiffness of this sensor is 1 N/μm, thus most of the loading stage deformation is actually taking place within the force sensor. We employ a laser (Keyence IL-S025), range 10 mm and resolution 0.1 μm, to measure the displacement of the PMMA plate, d_P (Figure 2). For all the experiments, we keep the initial value of d_P the same to ensure each fault slip starts from the same position.

Prior to performing the experiments, we fix the PMMA plate to the aluminum frame and attach the silicone block to the rigid steel base and clamp it. We use a digital level to make sure that the whole experimental system, especially the slip plane, is flat horizontal. Each experiment begins at the moment when the shear force starts to increase on the PMMA plate, given the analog fault has been previously loaded by a stable normal load. The duration of each experiment is set to 600 s. We performed 28 experiments by applying various normal loads and displacement rates (Table S1 in Supporting Information S1). We define the x-direction as the sliding direction of the PMMA plate while the direction y is set perpendicular to the x-direction.

To demonstrate the transition from steady slip to stick-slip in our analog fault system, the evolution of the shear force, F_S, under multiple normal loads, F_N, maintaining the same loading rate V_S of 5.0 μm/s is presented in Figure 4. We clearly observe the steady sliding of the interface when the normal load is quite small (e.g., F_N = 10 N). On the other hand, multiple stick-slips are observed when the normal load becomes greater than 50 N (Figure 4). In addition, the shear force drop of each stick-slip increases with the increase of the normal load.

2.3. Optical Monitoring

To capture the positions of asperities and compute their slips during the experiments, we use a high-resolution camera (Nikon D800) with a lens (Nikon 105 mm f/2.8D AF Micro-Nikkor) in automatic focus mode to record videos. A mirror fixed inside the aluminum frame, which is inclined at 45°, reflects the interface and moves with the sliding of the PMMA plate during the experiments (Figure 2). The main settings of the optical system are as follows: aperture size f/14, exposure time 1/30 s, and photosensitivity (ISO) 100. Two LED lights are placed behind the camera to supplement sufficient light for the clear observation of the interface. We record videos of dimensions in 1,920 × 1,080 pixels with a sampling rate of 29.97 frames per second. In addition, to synchronize the force measurement and the optical monitoring, we send an electrical synchronization signal and correct the time base of each record.

For each experiment, we extract all pictures taken by the camera between the times t_0 and t_f which are, respectively, the times at the beginning and the end of an experiment. From this set of pictures, we extract the slip of each individual asperity as a function of time. Denoting $x_i(t)$ and $y_i(t)$ the positions of the center of asperity i in a fixed reference frame (attached to the ground) we can define the displacement, $d_i(t)$, of an asperity along the loading direction in this fixed frame,

$$d_i(t) = x_i(t) - x_i(t_0). \quad (1)$$

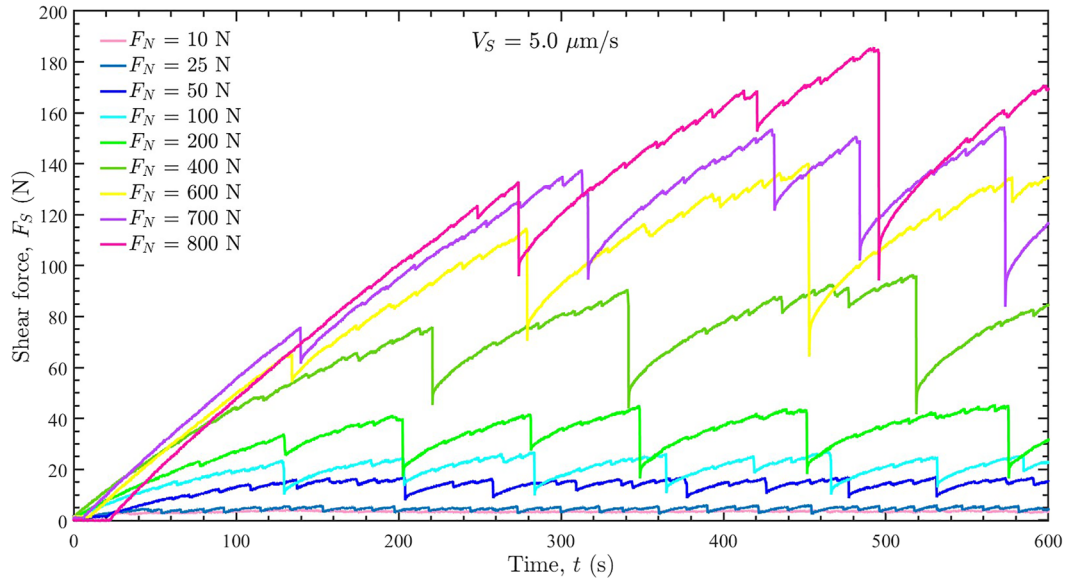

Figure 4. Temporal evolution of the shear force under multiple normal loads. The interface slips steadily when the normal load is quite small while evident stick-slips occur when the normal load becomes greater than 50 N. With the increase of the normal load, the shear force drop also increases.

Similarly, we define $x_P(t)$ as the position of the center of the mirror in the same fixed frame and then its displacement (which corresponds to the displacement of the PMMA plate as well), is computed as:

$$d_P(t) = x_P(t) - x_P(t_0). \tag{2}$$

The cumulative slip of asperity i at time t is defined as the difference of the displacement between the two sides of the interface (i.e., the asperity and the PMMA plate):

$$u_i(t) = d_i(t) - d_P(t). \tag{3}$$

As the camera and the silicone block are both fixed to the ground while the mirror moves with the sliding PMMA plate, the position of each asperity, i, on pictures taken by the camera is relative to the moving frame of the mirror and is noted $\left(x_i^*(t), y_i^*(t)\right)$. It follows that the displacement of an asperity in this moving frame is simply $d_i^*(t) = x_i^*(t) - x_i^*(t_0)$. From the definition of the cumulative slip introduced before, this displacement, $d_i^*(t)$, corresponds exactly to the cumulative slip, $u_i(t)$ of asperity i. Consequently, the cumulative slip of each asperity is obtained by tracking the evolution of its position, $x_i^*(t)$, between time t_0 and time t_f.

We developed a two steps procedure for tracking the evolution of the position $x_i^*(t)$ of each asperity i in the moving frame of the mirror. In the first step, we applied the circular Hough transform algorithm implemented within MATLAB for automatically detecting circular objects (Davies, 2005; Yuen et al., 1990). From the first and last pictures at times t_0 and t_f respectively, we extract the initial position $x_i^*(t_0)$ and final position $x_i^*(t_f)$ of asperity i. We also estimate the initial position of the beads, $y_i^*(t_0)$ in the direction perpendicular to the slip direction.

The initial positions of asperities detected at time t_0 are shown in Figure 5. The asperities marked by red circles, with a total number of $N = 144$, are retained in our analysis while the asperities with blue markers are excluded from the subsequent image analysis because they are located too close to one of the image edges. We note the value of N may change with different experiments mainly due to the field view of the camera, but it fluctuates around 140. In addition, we obtain the radius R, which is 36 pixels, and compute the scaling of the image from the known radius of the PMMA beads ($R = 3$ mm), 12 pixels/mm. Based on the initial and final positions of asperities, we are able to estimate the total slip $u_i^*(t_f) = x_i^*(t_f) - x_i^*(t_0)$ of each asperity. Due to the constant loading rate, a simple linear trend between these two positions gives an approximate position, $x_i^*(t)$ of asperity i at each time step. This provides a first-order estimate of each asperity location during the experiment. In the second step, in order to obtain the most accurate locations, we applied an image correlation technique (Sutton et al., 2009) to refine these first measurements.

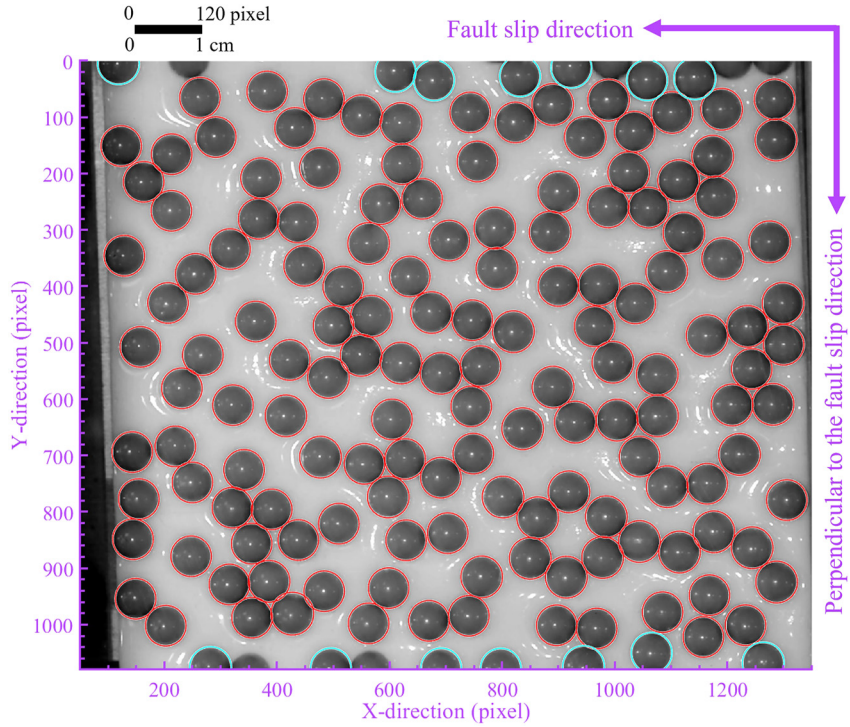

Figure 5. Typical automatic detection results indicating the initial positions of asperities at time t_0, on the interface within a region of interest of dimensions 1,300 × 1,080 pixels (i.e., 108.33 × 90 mm). The asperities without markers represent the undetected ones while the asperities with blue circles correspond to the excluded ones as their correlation windows exceed the image boundary. A total of $N = 144$ asperities marked by red circles are kept and their positions $x_i^*(t_0)$ are taken as the initial positions for computing the slip through the image correlation.

To quantify the slip of each asperity, a square window for image correlation with a size of $\sqrt{2}R$ is defined at the center of each asperity based on our previous estimates of $x_i^*(t_0)$ and $y_i^*(t_0)$. We extract the image defined by the square correlation window of each asperity at all frames. For each asperity, we compute the FFT (fast Fourier transform)-based two-dimensional cross-correlation between the extracted window defined at time t_k and the window defined at time t_{k-1}. From the correlation map, we isolate the position of the maximum value which gives the displacement of the bead. We then shift the correlation window of the second frame based on this displacement and repeat the procedure until the computed displacement is null. At this last stage, we then extract a sub-sample displacement by interpolating the correlation map around its maximum. The final displacement of the bead between the two time frames is then obtained by summing all displacements computed during this iterative process. Repeating this procedure for all time frames and for each bead we are able to obtain the cumulative slip of each asperity during the whole duration of an experiment. The typical resolution of the resolved displacement in each direction is of the order of 0.01 mm.

Due to the geometry of our experimental setup, the non-parallelism which may result from the non-perfect 45-° inclination of the mirror and/or the non-parallel view between the camera lens and the slip plane (Figure 2), can create a non-linear scaling along the x axis. In order to eliminate this effect, we correct the cumulative slip of asperity i based on its total slip $u_i(t_f)$, which is supposed to be no greater than the displacement $d_P(t_f)$ of the PMMA plate at time t_f. Given the corrected cumulative slip $u_i(t)$ of asperities, we then update the displacement $d_i(t)$ of asperities following Equation (3).

Finally, we also note that the asperities also exhibit slips perpendicular to the loading direction. These cumulative slips are near-evenly distributed around zero and the maximum cumulative slip is quite small compared to the cumulative slip along the faulting direction. We present the trajectories of all the asperities during the whole experimental duration in Figure 6, where the onset of the trajectory of each asperity is set to be at the origin (0,0). The total slip during this experiment is of the order of the asperity size, $R = 3$ mm, and the slip in the x direction is about 10 times larger than that in the y direction. There is a fan shape of the trajectories with a mean y-direction

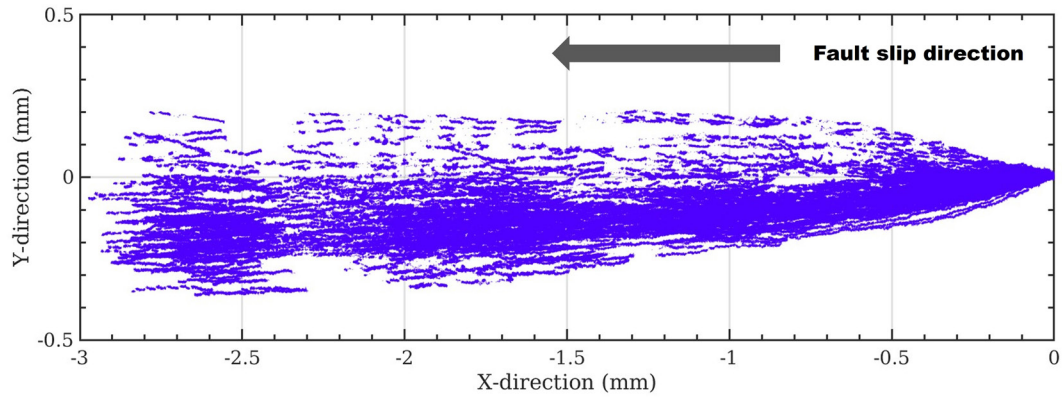

Figure 6. Trajectories of all the asperities during the whole duration of an experiment under a normal load of 400 N and a loading rate of 5 μm/s. The onset of each trajectory is superimposed to be at the origin (0,0). The prominent gaps correspond to the large stick-slip events.

that is close to zero. We observe several prominent gaps that correspond to the large stick-slip events (LSEs) during the faulting. For the other experiments under different loading characteristics, the total slip of asperities in the x direction is dependent on the loading rate and the experimental duration while that in the y direction is generally of the same order of ∼0.3 mm.

3. Collective Behavior of Asperities

3.1. Temporal Evolution of the Cumulative Slips of Asperities

To understand the individual behaviors of asperities as well as the relationship between each local asperity and the whole interface, we present the temporal evolution of the cumulative slips of individual asperities. For a better visibility, only 20 asperities, randomly selected out of 144 asperities, are presented in Figure 7. The cumulative slips of the 20 asperities are color-coded by their initial positions $y_i(t_0)$. We also indicate in Figure 7 the loading rate of the interface which is 15.0 μm/s here. Any asperity following this trend could be considered then as fully sliding. On the contrary, a fully sticking asperity would accumulate no relative slip with respect to the loading plate. Its behavior would appear as a horizontal line in Figure 7.

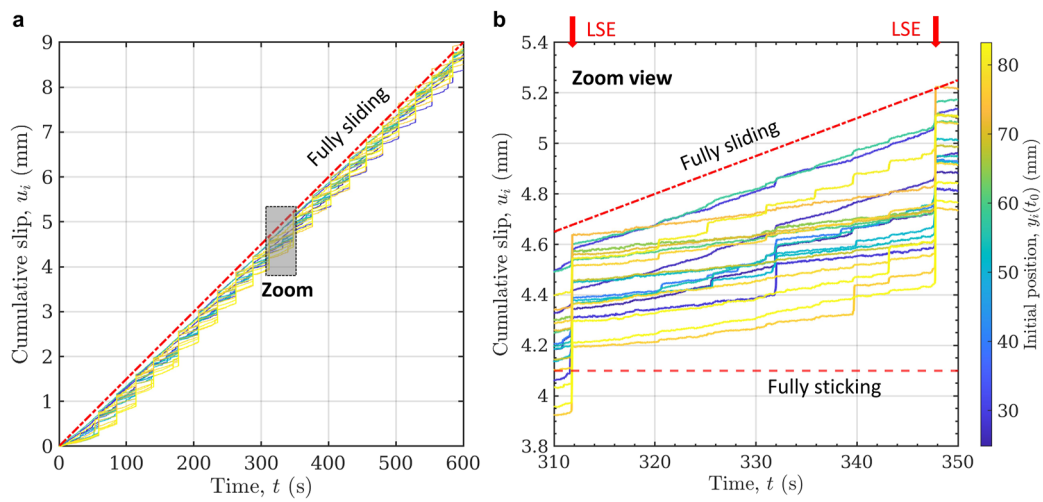

Figure 7. (a) Temporal evolution of the cumulative slip in the x direction for 20 asperities during an experiment under a normal load of 200 N and a loading rate of 15.0 μm/s. The cumulative slips of the 20 asperities are colored-coded by their initial y positions at time t_0. (b) Zoom view of (a) showing the detailed behaviors of asperities during one time interval between two large stick-slip events (LSE) and ranging from 310 to 350 s. Fully sticking indicates a locked state while fully sliding gives the slope of the imposed displacement rate to the system.

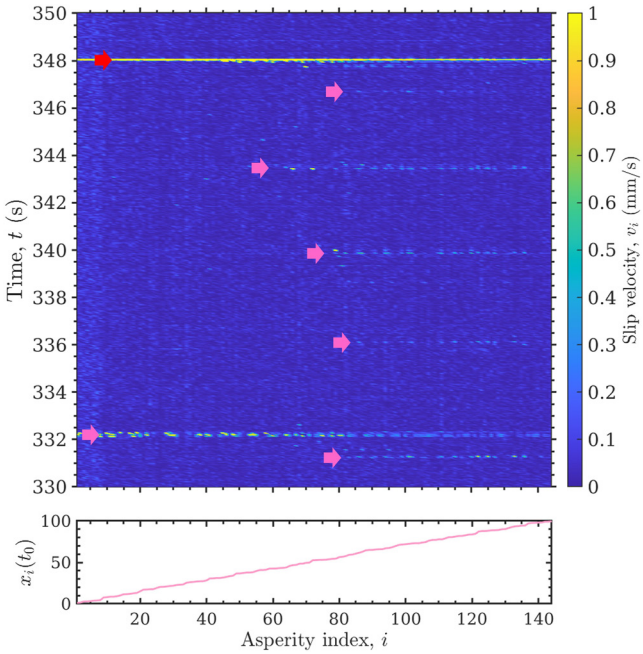

Figure 8. Slip velocity of all the asperities during the time period ranging from 330 to 350 s of the same experiment shown in Figure 7. The asperities are sorted in ascending order by their initial x positions at time t_0, $x_i(t_0)$. A large stick-slip event (LSE) indicated by the red arrow occurred at time 348 s observed, where all the asperities are synchronously slipping. During the sticking phase, there are also several small stick-slip events (SEs) which are indicated by the pink arrows involving the slipping of a part of asperities. We note that the slip velocity is thresholded as 1 mm/s to clearly show the slipping of local asperities. The maximum slip velocity is about 11 mm/s which is a rough proxy as this might be strongly sensitive to the sampling rate of the camera.

The stepping feature of cumulative slip evolution of the asperities in Figure 7 illustrates the repetitive stick-slip events of the interface (20 events in Figures 7a and 7a zoom on one of them in Figure 7b). These events involve all the asperities of the interface. In the time interval between these whole stick-slip episodes, during the sticking phase, the asperities show distinct behaviors. We observe that all the slipping rates are smaller than that of imposed loading rate (see the slopes of the cumulative slip of the asperities and the PMMA plate) but with a non-horizontal trend, which indicates that, actually, the asperities are slipping at a low rate during the sticking phase, instead of being fully locked.

It is noteworthy that the slips accumulated during each sticking period are not the same for different asperities. This proves that different asperities can slip at different rates, though they are all in the quasi-static regime (i.e., the sticking phase of the interface stick-slip behavior). Another interesting finding is that there are also some small visible slips that occurred at different single asperities during the overall sticking phase and correspond to small stick-slip events at the scale of several asperities. These small episodes contrast with global slip episodes, when all the local asperities slip rapidly in a synchronous way and that we define as a LSE. Moreover, the observation that the slips on all asperities after a LSE do not reach the imposed loading slip, indicates that accumulated stress is only partly released during such a whole scale event.

3.2. Slip Velocity of Asperities

Slip velocity reflects the slipping rate of asperities, which is estimated using a given discretization of the time (i.e., time step) during the whole experiment. The slip velocity $v_i(t_k)$ of each asperity i is computed as

$$v_i(t_k) = \frac{s_i(t_k)}{\Delta t} = \frac{u_i(t_k) - u_i(t_{k-1})}{\Delta t}, \tag{4}$$

where $s_i(t_k)$ is the slip of the asperity i at time t_k and Δt is the fixed time step of 1/29.97 s determined by the sampling rate of the camera, that is, $t_k - t_{k-1}$. Following the same experimental data used in Figure 7, for illustration, the slip velocity of all the 144 asperities ranging from time 330 s to time 350 s is shown in Figure 8, where the asperities are sorted in ascending order by their initial positions $x_i(t_0)$. A LSE involving the synchronous slipping of all the asperities is observed at the time 348 s. We also observe several small stick-slip events that share the same characteristic, which is the synchronized sliding of only a part of the asperities.

3.3. Mechanical Response of the Interface

In order to document the mechanical response of the frictional interface, we analyze how the shear force evolves as a function of slip. Here we define the shear-to-normal force ratio, $\mu_f = F_S/F_N$, as the effective friction coefficient during the slip of the sticking phase, while the shear-to-normal force ratio, $\mu = F_S/F_N$, is defined as the friction coefficient at the onset of a LSE. We compute the spatial average of the cumulative slip, $\langle u(t) \rangle$, over all asperities, N, following

$$\langle u(t) \rangle = \frac{1}{N} \sum_{i=1}^{N} u_i(t), \tag{5}$$

which is a global indicator of the collective behavior of all the asperities. As multiple seismic cycles (i.e., LSEs) are produced during a single experiment, we report in Figure 9a the evolution of μ_f as a function of $\langle u(t) \rangle$, for all the cycles of a single experiment. Each cycle is separated based on the onset of a large scale slip event LSE (observed when μ_f reaches a local maximum before an abrupt decrease, i.e., when $\mu_f = \mu$). The value of the friction coefficient mainly ranges between 0.10 and 0.23, which is a low value but comparable to the values in

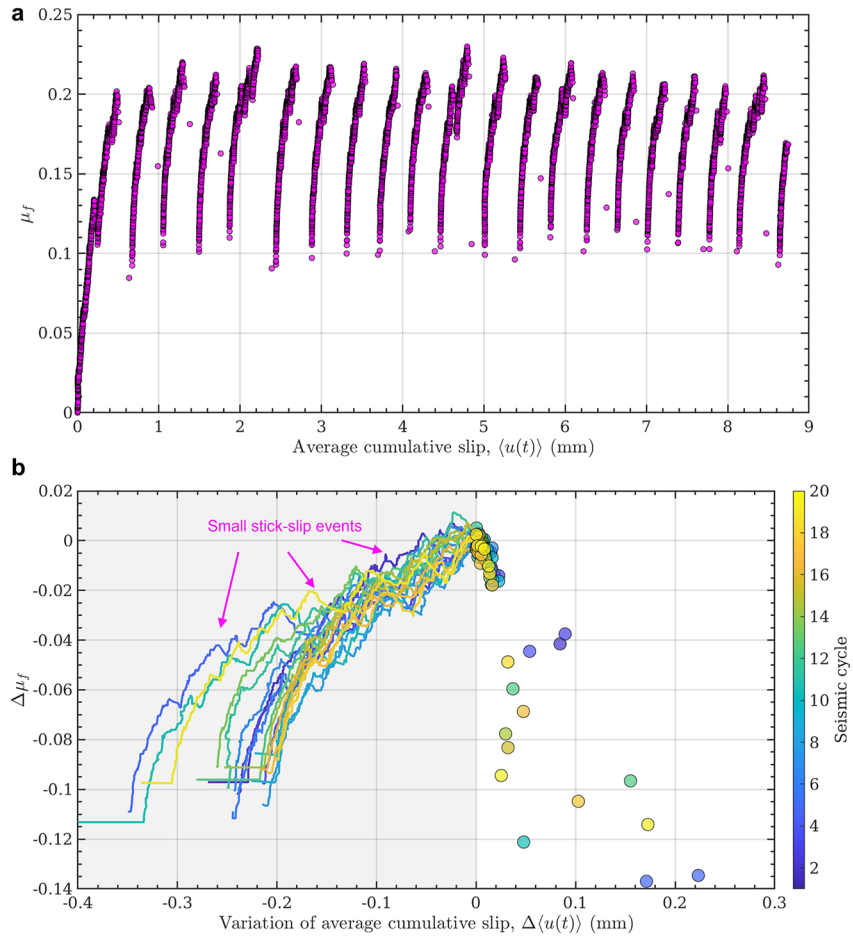

Figure 9. (a) Evolution of the shear-to-normal force ratio, μ_f, as a function of the average cumulative slip, $\langle u(t)\rangle$, during the same experiment shown in Figure 7 with multiple seismic cycles. (b) Variation of the effective friction coefficient, $\Delta\mu_f$, as a function of the variation of the average cumulative slip of all the asperities, $\Delta\langle u(t)\rangle$, for the same experiment shown in (a). All the seismic cycles represented by different colors are superimposed together by setting the onset of each fast slipping phase as the origin. The colored curves in the shadow indicate different slow slipping phases while the circles denote the corresponding fast slipping phases.

other PMMA-PMMA interfaces (Baumberger & Caroli, 2006; Selvadurai & Glaser, 2015). We observe, in each cycle, a stage with an overall increase of the effective friction coefficient, μ_f, during the slow slipping phase and a weakening stage during the fast slipping phase.

To focus on the slow slipping phase of the whole faulting process, the variations of the effective friction coefficient, $\Delta\mu_f$, and of the average cumulative slip, $\Delta\langle u(t)\rangle$, are both computed relative to their respective values at the onset of these large scale slips. We plot the variation of the effective friction coefficient, $\Delta\mu_f$, as a function of the variation of the average cumulative slip of all the asperities, $\Delta\langle u(t)\rangle$, by superimposing all the slow and the fast slipping phases, where each onset of the fast slipping phase is set to be $\Delta\mu_f = 0$ and $\Delta\langle u(t)\rangle = 0$ (Figure 9b). The curves represent the slow slipping phase while the circles represent only a few time steps after the onset of the large scale event (LSE). We observe a good similarity between all seismic cycles, proving the repeatability of our observations. We observe that the effective friction coefficient during the period preceding the LSE is increasing. This strengthening of the interface is occurring while the interface is slipping. We observe that during this overall increase of the effective friction coefficient, there exist multiple instances where μ_f actually drops significantly compared to the error of the effective friction coefficient measurement. The strengthening of the interface (an overall increase of μ_f) is thus not a homogeneous process and is slip-controlled in a non-linear manner. It should be noted that slip-strengthening is defined here at the global scale (i.e., the entire fault interface) as phenomenological behavior, that is, the increase in frictional strength with mean interface slip. This definition of slip-strengthening

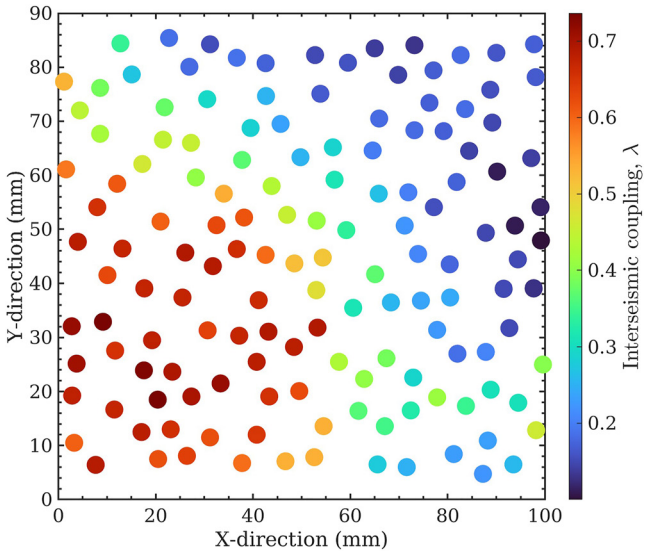

Figure 10. Map of the interseismic coupling of asperities along the interface using the same experimental data shown in Figure 9. A similar pattern between the peak heights of asperity (Figure 3b) and the interseismic coupling is observed, which shows that a larger peak height corresponds to a larger interseismic coupling whereas a smaller peak height corresponds to a lower interseismic coupling.

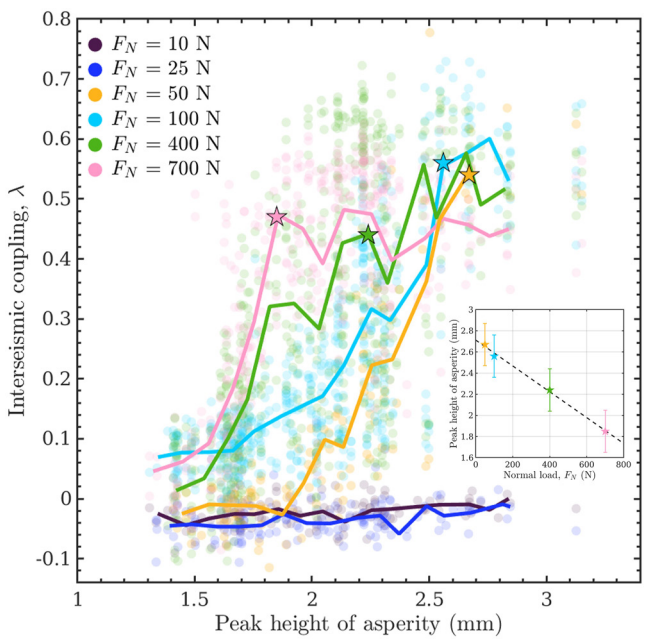

Figure 11. Evolution of the interseismic coupling at different peak heights of asperity under multiple normal loads. The circles with one filled color are the dataset computed for all the experiments under the corresponding normal load. Each curve is obtained by averaging the interseismic coupling over the peak height of asperity with a bin width of 0.10 mm. The inset displays the peak height of asperity at transitions from high to low coupling (stars) as a function of the normal load, where the peak height of asperity decreases with the increase of the normal load.

also applies elsewhere in this paper (e.g., key points, discussion, etc.). This shows as well that this slip-strengthening stage, conventionally considered as the stable regime of a fault, actually consists of many small-scale destabilizing events. The rapid slip that occurs during a LSE is not well captured by our experiments mainly because of the limited time resolution of the camera that does not allow a sufficient time sampling during this stage. It is also possible that the weakening part is velocity dependent which is not well captured here since Figure 9b represents the effective friction coefficient, μ_f, as a function of slip with no information on the velocity.

3.4. Topographical Effect on Interseismic Slipping Behaviors

Our results show that many small stick-slip events accompanied by effective friction coefficient drops are found during every slip-strengthening stage (Figure 9). These interseismic, small stick-slip events result from the slip of a limited number of asperities on the interface. In order to identify what controls the number and the amount of these partial slips, we document the interseismic slipping behaviors of the asperity using the interseismic coupling coefficient (Hyndman et al., 1997). We denote the onset times of the j and the $j+1$ LSEs as $t(\mathrm{LSE}(j))$ and $t(\mathrm{LSE}(j+1))$, respectively. To describe the extent of the slipping of the asperity i during the interseismic phase between $t(\mathrm{LSE}(j))$ and $t(\mathrm{LSE}(j+1))$, the interseismic coupling, $\lambda_{i,j+1}$, is computed as

$$\lambda_{i,j+1} = 1 - \frac{u_i(t(\mathrm{LSE}(j+1))) - u_i(t(\mathrm{LSE}(j)))}{d_P(t(\mathrm{LSE}(j+1))) - d_P(t(\mathrm{LSE}(j)))}. \quad (6)$$

We note that λ is in the range [0, 1], where $\lambda = 0$ indicates no coupling or fully sliding while $\lambda = 1$ denotes a fully coupled interface or sticking. For experiments with multiple seismic cycles, we compute the final interseismic coupling for each asperity i by averaging λ_i over all of the interseismic phases. With the experimental data used in Figure 9, we present the interseismic coupling of these asperities along the interface (Figure 10). We observe a large scale trend of this interseismic coupling that we can link with the same trend observed from the peak height of asperity derived from the topographical map (Figure 3b). A higher peak height of asperity corresponds to a higher interseismic coupling while a smaller peak height is corresponding to a lower interseismic coupling. This can be interpreted in terms of normal stress on the asperity where a higher peak height causes a greater normal stress, and therefore creates the locking of the asperity which increases the interseismic coupling. On the contrary, the asperities with smaller peak heights have a low normal stress and thus cannot accumulate large shear stress (and consequently large slip deficit) and will fail more often during the interseismic phase and have a low coupling, that is, low values of λ.

We also investigate the direct effect of the macroscopic normal load on the interseismic coupling, as shown in Figure 11. For all experiments with the same normal load, we compute the interseismic coupling of each asperity, which is indicated by the colored circles. The average evolution of the interseismic coupling with peak heights conceals some scattering. Indeed, we can observe from Figure 11 that for the same normal load and the same asperity height, different values of λ are computed. To present the evolution of the interseismic coupling as a function of the peak height of asperity, we average the interseismic coupling values over peak heights within a bin width of 0.10 mm. It evidences that, when the normal load is low: 10 and 25 N, all the asperities have a quite small interseismic coupling, a value that is not

distinguishable from zero. The interseismic coupling shows no dependency on the peak height. This is consistent with the mechanical response of the fault system shown in Figure 4, where the global fault slips almost steadily under the normal loads of 10 and 25 N.

As the normal load increases and becomes large enough such that large stick-slips of the whole fault system are observed, we evidence that interseismic coupling is then dependent on the peak height of asperities. The asperities with low peak heights correspond to low normal stresses, thus inducing the small stick-slip events observed in between the LSEs due to a small interseismic coupling. For the same peak height of asperity, the interseismic coupling increases with the increase of normal stress, which strengthens the locking of the asperities. The maximum value of the interseismic coupling is about 0.55 which is significantly lower than 1. This is consistent with the partial slipping of asperities shown in Figures 7b and 8. It is interesting to note a transition of the interseismic coupling, for a given normal load, at a specific peak height threshold. This peak height threshold is decreasing as a function of the increased normal stress (from about 2.67 mm at 50 N to about 1.85 mm at 700 N). The interseismic coupling above this peak height threshold converges for all loading conditions to a constant value of around 0.6. Below the threshold, λ decreases toward 0.

4. Interactions Between Asperities During the Slip-Strengthening Phase

4.1. Collective Slip Episodes

To investigate the spatiotemporal interactions of asperities, we use a two-step procedure in order to define and characterize slip episodes (SEs). In the first step, we analyze individually each asperity to isolate individual asperity slips (IASs) from their slip history. In the second step, we identify collective behavior by clustering IASs based on their time and space connection to build slip episodes. The first step is realized by thresholding the velocity $v_i(t)$ for each asperity i. We use a threshold Γ_i specifically for each asperity i, which is determined by considering the median $\tilde{v}_i$ and the median absolute deviation D_i^{med} of the slip velocity $v_i(t)$,

$$\Gamma_i = \tilde{v}_i + c \cdot D_i^{med}, \tag{7}$$

We test several values of the coefficient c in front of D_i^{med} (see Figure S2 in Supporting Information S1) and found that the value retained here ($c = 6$) is best able to separate noise from slip event. Following Equation 7, we define the IASs as periods with $v_i(t) > \Gamma_i$ while the others with $v_i(t) \leq \Gamma_i$ are taken as minor slip events and possible noise, and are not included in the catalog of IASs. Figure 12 presents the slip events (blue stars) of one single asperity ($i = 98$) for the same experiment displayed in Figure 7 and its corresponding threshold Γ_{98} (thick magenta line). We find a diversity of slip velocities of IASs. To display the IASs with low slip velocities during the interseismic phase, we zoom in on Figure 12 during a time interval between two LSEs, ranging from 310 to 350 s (the same time period exhibited in Figure 7b). The observation that several IASs with moderate maximum slip velocity are observed for this asperity is actually consistent with the small stick-slip events found during the slip-strengthening stage shown in Figure 9. For each experiment, we establish a complete catalog of IASs by computing the slip velocity $v_i(t)$ of all the asperities and the corresponding threshold Γ_i.

To cluster in space and time all the IASs defined at different asperities into collective SEs covering multiple asperities and time steps, we analyze the time and space connections of these IASs. We define a link between a pair of IASs if the two events are separated in time by one or less time step and if they have a spatial connection (i.e., they are nearest neighbor), introducing a two-dimensional Delaunay triangulation, and considering the location of each asperity as a vertex (Lee & Schachter, 1980). The edges of the resulting triangulation give the spatial connection between asperities used to make clusters. Additionally, we assume that an asperity is always spatially linked with itself. The IASs simultaneously connected in time and space scales are clustered as a new SE using a single linkage clustering algorithm (Gan et al., 2020). IASs that are not linked to other neighboring IASs are considered as individual SEs. Figure S3 in Supporting Information S1 shows one SE lasting only one time step, and composed of nine IASs. The polygons with different colors represent the slip area allocated to each IAS and are determined by the Voronoi diagram corresponding to the performed triangulation (Fortune, 1995). We, therefore, are able to build the catalog of spatiotemporal SEs for each experiment.

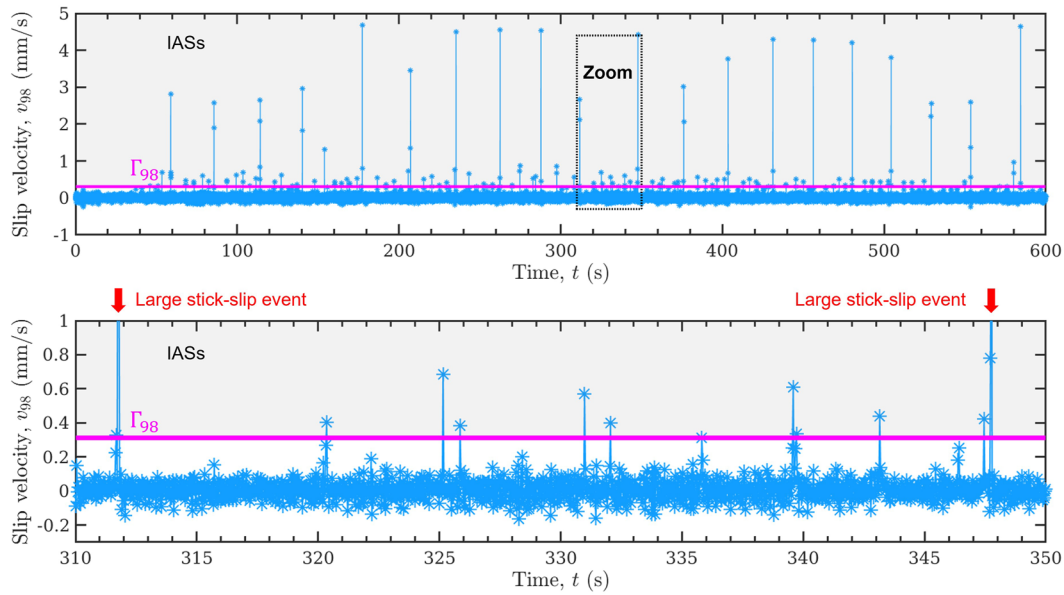

Figure 12. Time-localized slip events produced by a single asperity ($i = 98$) in the same experiment shown in Figure 7. The blue stars and the thick magenta line represent slip events and the corresponding threshold Γ_{98} specifically computed for this asperity. The slip events localized in the shadow region with slip velocity greater than the threshold are defined as IASs while the others indicating minor slip events and noise are removed. A zoom view showing the low amplitude IASs during an interseismic phase ranging from 310 to 350 s is presented below. Several IASs with low slip velocities are observed.

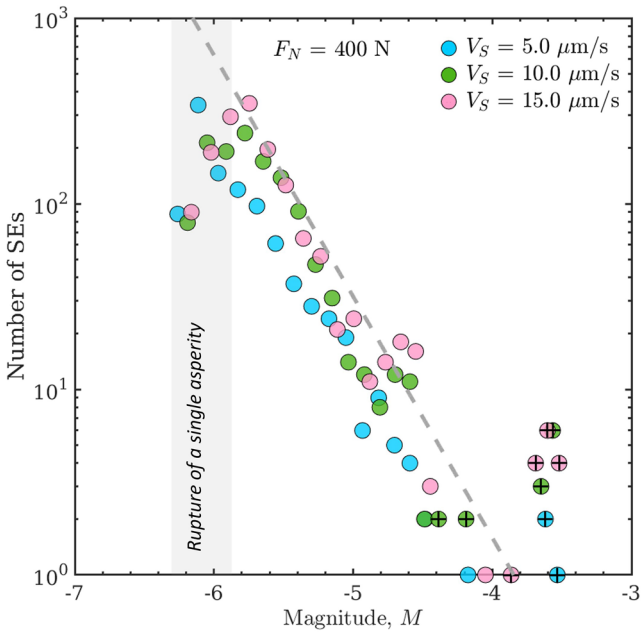

Figure 13. Magnitude-frequency distribution at different loading rates under the same normal load of 400 N. The circle symbols marked by crosses indicate the large stick-slip events at the global fault scale, which are excluded from the computation of the b value since they are reaching the boundaries of the model and accordingly are limited in size. The gray dashed line indicates a reference line with a b value of 1.3. The shadow represents the range of the magnitudes corresponding to the ruptures of a single asperity, with an average value of $M = -6.09$.

4.2. Magnitude-Frequency Distribution

In order to characterize the so-formed slip events, we first investigate their magnitude distribution. The magnitude of the slip event is estimated based on the computation of their moment, M_0. For one SE containing n IASs, its seismic moment is computed as:

$$M_0 = \sum_{i=1}^{n} G \cdot A_i \cdot s_i, \tag{8}$$

where G is the shear modulus of the PMMA, A_i and s_i are, respectively, the slip area and the slip of each IAS i that compose this SE. We note that the slip area, A_i, defined here is the effective slip area rather than the real slip area during an IAS since there is no frictional contact between asperities in our model. The estimation of such effective slip area, due to the difficulty of determining the discontinuity of slip zones, also exists when studying natural earthquakes originating from faults at depth. Another ambiguity comes from the selection of the shear modulus in Equation (8) as the analog fault interface is composed of bimaterial, that is, PMMA and silicone with different shear moduli. We thus emphasize that the moment computed here should be interpreted as relative values, instead of absolute values. More details about the definition of the slip area, the computation of the moment, and the choice of the shear modulus, will be further discussed in Section 5.5. Then, we can calculate the magnitude M of each SE following (Hanks & Kanamori, 1979) as:

$$M = \left(\log_{10} M_0 - 9.05\right)/1.5. \tag{9}$$

The magnitude-frequency distributions of the SEs extracted from three experiments, which are under the same normal load of 400 N but with three different loading rates, are presented in Figure 13. The shadow region marks

the magnitudes of the ruptures of a single asperity in these three experiments, with a range of $M = -6.09 \pm 0.22$. The symbols with crosses represent the LSEs that involve all the asperities of the interface and subsequently with a size controlled by the finite size of the interface. As evidenced already for finite systems, the distribution of events is bimodal: exponentially distributed size for the events not reaching the interface and a peak for system-wide events (Fisher et al., 1997). Excluding system-wide events, the observed distributions follow a typical Gutenberg-Richter distribution (Gutenberg & Richter, 1944): $\log_{10} N(m) = a - bm$. For the three experiments under loading rates of 5.0 μm/s, 10.0 μm/s, and 15.0 μm/s and a normal load $F_N = 400$ N, their b values and corresponding uncertainties are estimated as 1.21 ± 0.04, 1.49 ± 0.10, and 1.33 ± 0.13, respectively, using the maximum likelihood method (Aki, 1965). A gray dashed line showing a reference b value of 1.3 is displayed in Figure 13. We can observe that all these three experiments have a b value nearly similar to this reference. It shows that the b value has no clear dependence on the loading rate of the system. In addition, our experimental results show that the b value is insensitive as well to the imposed normal load (Figure S3 and Table S2 in Supporting Information S1). Such observation seems to be contradictory to the previous studies on natural faults and laboratory faults which have shown that the b value is dependent on the imposed stress (Amitrano, 2003; Rivière et al., 2018; Scholz, 2015). We however speculate that the limited range of tested normal loads, and the uncertainties attached to the b value, cannot provide a sufficient resolution to evidence a clear dependency of the b value on the imposed normal load.

4.3. Moment-Duration Scaling Relation

For regular earthquakes, a scaling relation between the moment and the duration is commonly observed and takes the form $M_0 \propto T^3$ (Kanamori & Anderson, 1975). This relation can be understood from the representation of an earthquake as a circular crack expanding at a constant speed and with a constant stress drop. Another scaling relation has also been resolved for slow slip events observed in subduction megathrusts which follows the form $M_0 \propto T$ (Gao et al., 2012; Ide et al., 2007).

We represent from our SEs the relation between their duration, T, defined as the time difference between its onset and end, and their moment, M_0, for all experiments with various normal loads and loading rates (Figure 14a). Two populations of SEs, where one is the small and moderate SEs in blue and another is the large SEs in red, are evidenced.

In order to retain in this analysis only confined ruptures and not be influenced by the condition at the edge of the sample, we set a threshold of 2.8×10^3 mm^2 by considering the slip area of SEs to exclude the large slip events reaching the edge of the sample. We evidence a linear scaling relation close to $M_0 \propto T$ for all the experiments for $M_0 < 100$ N m and a transition to the scaling for earthquakes ($M_0 \propto T^3$) for the large events (Figure 14b). We note that such a transition mainly results from the value of the threshold as some confined and unconfined events might be mixed. By changing the value of the slip area threshold, we observe that the linear scaling relation becomes more evident with the decrease of the threshold (Figures S5 to S8 and Figures S9 to S12 in Supporting Information S1). Thus, we conclude that the scaling of the small and moderate events (compared to the system size) is in $M_0 \propto T$ and not in $M_0 \propto T^3$ which is an artifact of the existence of two populations. The moments corresponding to the ruptures of a single asperity are marked by the shadow region, with a range of $M_0 = 2.32 \pm 0.91$ N m, which is also compatible with the magnitudes shown in Figure 13. Additionally, we find that such a scaling relation is also insensitive to the imposed normal load (Figures S5 to S8 in Supporting Information S1) and the loading rate (Figures S9 to S12 in Supporting Information S1). We still note however that the fitted range of duration is limited and further experiments with a wider range of event duration would be helpful to reinforce this result.

Excluding the large slip events reaching the edge of the sample by using the same slip area threshold (2.8×10^3 mm^2), we then compute the distance between the first and last slipping asperities for each retained SE. The duration and expanding distance are averaged to present their relation, as shown in Figure 14c. We observe a square-root scaling relation between the expanding distance and the duration.

4.4. Temporal Decay of Slip Episodes

In order to investigate the possible time interaction between our identified SEs, we compute the time correlation between them, $C(t)$ with

$$C(t) = \frac{1}{T n_t} \sum_{i=1}^{n_t} \sum_{j=i+1}^{n} \Theta(t_j - t_i \in [t; t+T]), \tag{10}$$

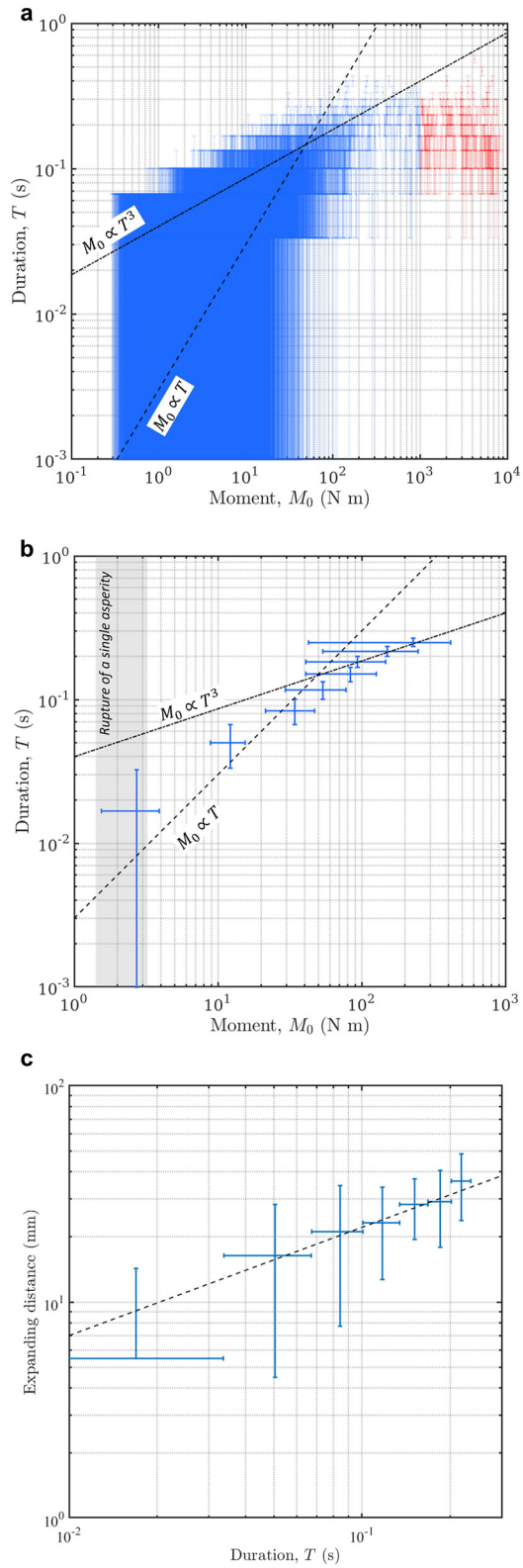

Figure 14.

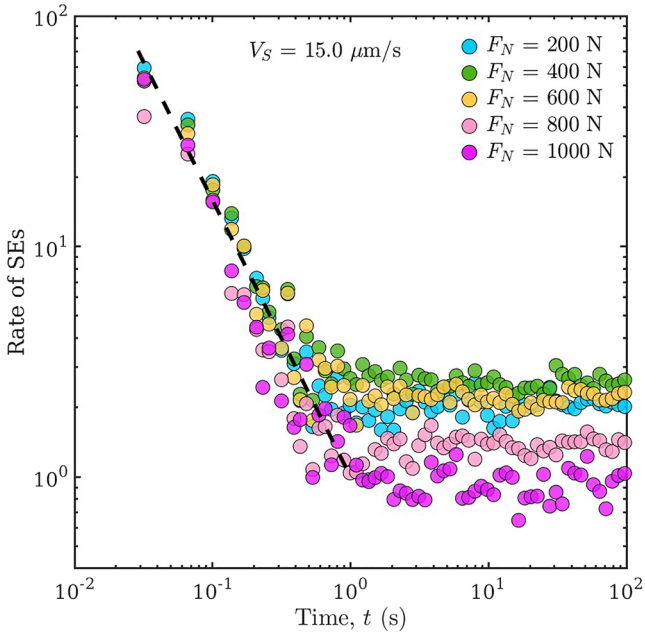

Figure 15. Temporal decay of SEs defined in multiple experiments under different normal loads and the same loading rate of 15 μm/s. The rate of SEs first decays rapidly with 1/t during about 1 s and then keeps stable as a background value of about 1 or 2 SE(s) per second.

where $\Theta(\mathcal{P})$ of proposition $\mathcal{P}$ is one if $\mathcal{P}$ is true and 0 otherwise. In order to take into account the time finiteness of the catalog, the first sum is performed up to n_t which is the largest index i such that $t_n - t_i < t + T$, where T is the duration of the time bin. Equation (10) actually gives the average rate of SEs at time t following a preceding slip event. We represent examples of $C(t)$ computed for multiple experiments under different normal loads and the same loading rate (Figure 15). We observe that, for all of these experiments, a rapid decrease of $C(t)$ at a short time range, following a power law decay similar to 1/t. After a duration of about 1 s, the average rate of SE stabilizes to a background rate of around 1 or 2 SE(s) per second. This indicates that interactions between SE exist for a short time and that they quickly decay. This evolution of the event's rate bears some analogy with Omori's law observed after large earthquakes or LFEs which gives as well a decay of the earthquake rate following 1/t (Lengliné et al., 2017; Utsu et al., 1995). The observation of the same decay rate under different normal loads indicates that the decay rate has no clear dependency on the imposed normal load. Our experimental results also show that the decay rate is independent of the loading rate (Figure S12 in Supporting Information S1).

5. Discussion

5.1. Interseismic Coupling

Our results indicate that the interseismic slip rate relative to the loading rate, that is, the interseismic coupling, λ, is related at first order to the normal stress imposed on the asperities. The transition from small to high coupling is a function of the normal load (the height of the asperity at this transition is decreasing with normal stress) but the value of the coupling at high or low normal stress is the same for any normal load. This is visible first as a global macroscopic effect affecting all asperities when we change the imposed normal load in our experiments (Figure 11). This can also be observed at the individual asperity scale where we observe that the asperity peak height is correlated with λ. Indeed, considering a simple Hertz contact model, a higher asperity height results in higher normal stress. The distribution of asperity heights in our experiments, therefore, leads to a distribution of normal stresses and a continuum of values of λ (Figure 11).

It is tempting to relate the characteristic asperity height in our experiment to the critical reduction in the normal force, ΔF_N^*, that controls the transition from low to high coupling, as identified in the model of Scholz and Campos (1995); Scholz and Campos (2012). However, since the interface is regarded as homogeneous, it should be noted that in this model the transition is only caused by the impact of the global normal load. This approach is thus describing the effective seismic coupling of the interface but not that of the asperities, which we can achieve in our experiments. According to our interpretation, the fault's quenched disorder influences the interface's effective coupling, which is then indirectly influenced by the normal stress. For example, there wouldn't be any variation in interseismic coupling at various asperities if we assumed that all of the asperities were the same height. Therefore the whole interface would have the same behavior as that of the asperities. Here we emphasize that, in contrast to the traditional normal stress level effect, a fault topography with changes in asperity heights has an impact on the effective seismic coupling of the fault.

Finally, we acknowledge that the definition of interseismic coupling is not completely satisfactory as it fails to capture the variation of the slip velocity inferred on some asperities in between two large scale stick-slip events. Indeed, we highlighted some transient activity and non-steady slipping rate for asperities which indicate that the

Figure 14. (a) Moment-duration distribution obtained using SEs from all experiments at various normal loads and loading rates, with a slip area threshold of 1.0×10^4 mm^2 (i.e., the whole interface). The black dash-dotted line and dashed line represent the scaling relations of $M_0 \propto T^3$ and $M_0 \propto T$ for the guide, respectively. Two populations of events indicating small and moderate events (blue) and large events (red) are evidenced. (b) Average moment-duration scaling relation obtained using small and moderate SEs from all experiments as the large slip events reaching the edge of the sample have been excluded using a slip area threshold of 2.8×10^3 mm^2. The shadow indicates the moments corresponding to the ruptures of a single asperity, with a range of $M_0 = 2.32 \pm 0.91$ N m (c) Scaling relation between the expanding distance of SEs and their duration using the same dataset in (b). The black dashed line represents the square-root scaling relation between the expanding distance and the duration.

value we computed only represents an effective behavior of the asperity at the time scale between two large scale stick-slip events.

5.2. Interfacial Elastic Energy

Our results evidence that for an interface composed of multiple asperities, as in our system, local slip events with various sizes (see Figure 13) are taking place at all times. We also note that LSE that involve slips on all asperities of the interface are also observed. These large scale slip events can only happen when sufficient large stress has been accumulated on the strongest asperities. This requires that asperities at some time are synchronized such that initiating the failure at one location triggers the cascading rupture of all the asperities on the interface, thus generating the large scale stick-slip event. This is equivalent to a collective depinning (i.e., the transition of the physical system from a locked state to a slipping state Alava et al., 2006; Perfettini et al., 2001) induced by the long range elastic interactions in a slowly (quasi-static) loaded system.

We quantitatively illustrate such synchronization effect by computing the evolution of the interfacial elastic energy, E_h, and of the bulk elastic energy, E_t, following the definition of Schmittbuhl et al. (1996). The interfacial elastic energy, E_h, is quantified through the sum of the relative distance between two asperities over all the spatial links defined by the two-dimensional Delaunay triangulation:

$$E_h(t) = K_N \sum_{k=1}^{D} (l_k(t) - l_k(t_0))^2, \tag{11}$$

where l_k is the relative distance computed through the x positions of two asperities linked spatially and D is the number of the spatial links between two asperities defined by the Delaunay triangulation. K_N is the compressive stiffness between asperities, computed through $K_N = E_s\langle d_{asp}\rangle$, where E_s denotes Young's modulus of the silicone block and $\langle d_{asp}\rangle$ is the average distance between asperities which estimated to be 6 mm. The interfacial elastic energy, E_h, actually quantifies the variance of the change of distance between neighboring asperities, thus is related to the elastic force interactions between asperities. The bulk elastic energy, E_t, is the total elastic energy stored on the interface through the global loading, which is characterized by the collective change in the absolute positions of all the asperities along the x direction:

$$E_t(t) = K_S \sum_{i=1}^{N} (d_i(t))^2, \tag{12}$$

where K_S is the shear stiffness estimated using $K_S = G_sL$. G_s is the shear modulus of the silicone block and is estimated from its Young's modulus, 1.1 MPa, while L is the size of the interface, 10 cm. N is the total number of asperities and d_i is the displacement of each asperity.

Such energies and the definition of links between close asperities originate in the reference spring array model of Burridge-Knopoff (Burridge & Knopoff, 1967; Carlson & Langer, 1989). However, our model is also different from the Burridge-Knopoff model which has only short-range elastic interactions as the silicone block induces long-range elastic interactions and viscous damping. We present the interfacial elastic energy, E_h, and the bulk elastic energy, E_t, as a function of the PMMA plate displacement, d_P, for different experiments with various normal loads but the same loading rate, as shown in Figure 16. We identify multiple large scale stick-slip events and the corresponding slip-strengthening phases from the large abrupt drops of E_t and the slow accumulation of E_t, respectively. We also observe a similar pattern for the evolution of E_h, which is equivalent to the direct measure of the spreading of the x positions of the asperities apart from their initial position where $E_h = 0$. Additionally, we observe a clear dependency of E_h and E_t on the normal load, which is consistent with the mechanical response of the fault system shown in Figure 4. With the increase of normal load, the interfacial elastic energy, E_h, and the bulk elastic energy, E_t, also increase.

Such evolution of the elastic energies during successive seismic cycles illustrates the disordering effect of asperities (i.e., the absence of correlation with their original positions (Alava et al., 2006) and the build-up of the elastic energy during the slip-strengthening phase. We interpret the rising E_h as the disordering process of asperities, that is the strong perturbation from the initial position which is supposed to be quenched in the system. The sticking phases correspond to a period of increase of E_h during which the asperities increase disordering, while a LSE

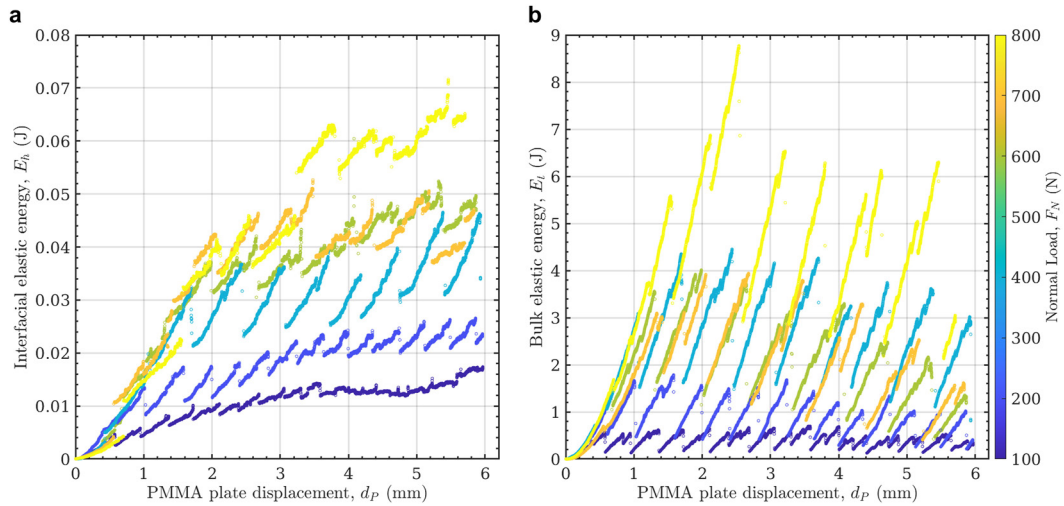

Figure 16. Evolution of (a) the interfacial elastic energy, E_h, and of (b) the bulk elastic energy, E_t, under different normal loads and the same loading rate. Both E_h and E_t accumulate slowly during the slip-strengthening phases and drop when a large stick-slip event occurs. Both E_h and E_t show a clear dependency on the normal load.

corresponds to the rapid decrease of E_h (re-ordering of the asperities). We note that during such a LSE, while E_t drops significantly and returns to zero, the drop of E_h is only partially such that a disorder, and elastic energy, is still present after a large event. It implies that there is a memory effect over the cycles from the relative positions of the asperities.

We also observe a transient period at the beginning of the shearing where the evolution of E_h is similar for all experiments. As the normal stress is increased a larger level of E_h is reached in the system, so a larger disordering of the asperities. It implies that higher normal stress prevents the interface to come back to its initial state (with low E_h) even during a LSE and so maintains a larger disorder in the system with internal stresses along the interface at any time.

The process of synchronization has been well documented notably in numerical simulations and shows that only for forces larger than a critical force, that constitute a critical point, the system will become unstable and sliding will extend to all sites of the interface (Albertini et al., 2021; De Geus et al., 2019; Fisher et al., 1997; Kammer et al., 2015; Tanguy et al., 1998). This constitutes a depinning transition and this phenomenology leads to stick-slip. In such models, this critical force is linked to a critical length scale, L_c, of an initiating slip pulse, that will invade all the interface if its extension becomes larger than L_c. Most of these results were inferred from a homogeneous fault model. Here, both the evolution of the macroscopic force (Figure 9) and the distribution of slip events in Figure 13 are not in agreement with these predictions. Indeed, we first observe in Figure 9 that the macroscopic force required to propagate a full scale event is not perfectly constant but rather displays some fluctuations from one rupture to the other. Secondly, the distribution of event magnitudes (Figure 13) shows almost no gap between the largest avalanche and the whole interface avalanche. It, therefore, implies that avalanches of all sizes can exist in the system without necessarily leading above a certain size to a complete failure. In such a case one would expect a larger gap in event size between the maximum observed avalanche and the system wide event. Such different nucleation mode can arise in the heterogeneous system as interactions between arrested small events could exist and significantly modifies the process leading to a major rupture (Albertini et al., 2021). Interpreting these results in terms of fault mechanics suggests that creeping faults correspond to the interface with an asperity disorder and a slip-strengthening regime with the disordering of the interface by small destabilizing events that increase elastic interaction between asperities but without impacting the global fault loading.

5.3. Slip Intermittency

Our system is driven by a constant displacement rate for each experiment and we measure a macroscopic velocity of the PMMA plate that is indeed constant (except during a large-scale event, where a small but noticeable displacement step is observed). This macroscopic measurement mimics the measure that could be made around natural faults by geodetic instruments located at the surface, and thus necessarily far away from the slipping area at depth. It implies that such kind of measurement actually misses the actual complexity of the slip distribution

taking place on the interface at a short time and spatial scale. Some fine measurements of the slip distribution in both time and space for shallow creeping faults indeed reveal that the long term continuous creeping of faults is actually accommodated during bursts of aseismic slip of various sizes (Jolivet et al., 2013, 2015; Khoshmanesh & Shirzaei, 2018; Rousset et al., 2016). During slow slip events, the analysis of GPS signal in conjunction with the recording of low frequency earthquakes (LFEs) also reveals that the large scale motion along the slab consists in the superposition of numerous small slip episodes each acting for a limited duration (Frank, 2016; Frank & Brodsky, 2019). The analysis of LFEs as a proxy for local slip on the interface reveals as well that these slip episodes span a wide range of sizes and present both temporal and spatial correlation (Lengliné et al., 2017). All these results are well in agreement with the observations performed in this study where the interseismic slip on the fault is characterized by slip events (SEs) of different sizes that act in a close temporal relationship.

The slip events we characterized here are slow events in the sense that the ratio of their size with respect to their duration is much lower than the Rayleigh wave speed of the material that constitutes the interface. Indeed, supposing a typical PMMA Rayleigh velocity of 1,255 m/s (Gvirtzman & Fineberg, 2021), this would imply that in one time frame (1/29.97 s) a dynamic rupture front travels up to 42 m. This is inconsistent with the observations of SEs that last several time frames. If we suppose that most of the stress transfer between asperities is actually mediated by the silicone base embedding the PMMA beads, this gives a Rayleigh wave velocity of the order of 20 m/s, and then the propagation of a rupture front of 66 cm in one time frame. As the largest SEs have a typical duration of 0.3 s and cover a maximum area with a characteristic dimension of half the sample length (5 cm), this suggests that the SEs formed by our criterion actually correspond to slow events. Such a slow process is achieved as the stress is mainly transmitted through the bulk of the silicone block due to the absence of frictional contact in between asperities, and could be damped by the bulk viscosity, which is similar to some numerical models composed of discrete frictional patches embedded in a viscous matrix (Ando et al., 2010, 2012; Behr et al., 2021; Nakata et al., 2011). It does not preclude local dynamic rupture to take place during such SEs, but their size might be limited to a single bead contact area (or smaller). This implies that the moment-duration scaling, we report in Figure 14 should be interpreted as scaling attached to slow ruptures on the interface. The best-resolved trend shows $M_0 \propto T$ in agreement notably with the observations of (Ide et al., 2007) that show that many slow slip events on subduction zones follow this scaling law. We note however that the scaling in our experiment is only resolved over a restricted range of moments. This calls for future further experiments involving an increase in the number of beads and the sampling rate of the optical device. This moment-duration scaling is also in agreement with the observed evolution of the slip event characteristic distance with the square root of duration. This, therefore, suggests that the slip events are driven by a diffusion process controlling the propagation of the rupture, similar to slow-slip events tracked with tremor migration (Ide, 2010). The recognition of these SEs as slow events also suggests that the magnitude-frequency distributions shown in Figure 13 can be considered as a scaling attached typically to such slow events as inferred, for example, from non-volcanic tremors (Wech et al., 2010), rather than a Gutenberg-Richter relation for ordinary earthquakes. The fact that the whole-fault-scale scaling relations presented by these slow events can be derived from the collective spatiotemporal slips of local asperities is also supported by some numerical studies of Ide (2008) and Ide and Yabe (2019). Additionally, the depinning transition leading to stick-slip constituted in the synchronization process is also consistent with the model of Ben-Zion (2012), which proposes that the depinning transition is a mechanism for the generation of tremors.

The slip event, SEs are characterized as a single rupture following the clustering procedure we defined. It is not obvious how to select the merging condition which is imposed partially in our case by the acquisition rate of the optical device. However, what is the exact definition and extent of a slip event is not a question limited to our experiment. Indeed, the analysis of earthquakes for example, generally indicates that they are actually composed of several sub-events. The identification of these sub-events, therefore, questioned the definition of the earthquake rupture that consists of several connected local slip episodes. As we discussed above, the same problem of definition arises for a slow slip event which is actually made of a sum of local transient slip episodes connected in time and space. Decreasing the time interval required to merge individual asperity slips into the same cluster would ultimately lead to only isolated local slip events. On the opposite, increasing this time interval would lead to a single slip event comprising all the beads. Finally, we conclude that SEs are thus analyzed at the spatial and temporal scale imposed by our acquisition system which is a constraint imposed as well to observations made on natural fault systems.

5.4. Mechanics of the Slip-Strengthening Regime

Our system resolves confined rupture that takes place during the slip-strengthening phase. This contrasts with most frictional setups where only large scale ruptures are analyzed during the weakening phase. Unlike these

large scale ruptures that are largely controlled by the machine loading stiffness (Leeman et al., 2016; Wu & McLaskey, 2019), partial ruptures provide the opportunity to study the slip events taking place on an interface without being actually influenced by the loading system. In our system, the events are arrested because of stress heterogeneity that arises notably from the variable asperity heights creating spatial differences in frictional strengths. We stress that the heterogeneous nature of the interface only arises as a result of the topography and the position distribution of the asperities with respect to their initial position (assessed by the interfacial elastic energy E_h), but that there is no variation of the material properties that constitute the interface. In particular, it implies that the complex dynamic that we recovered during our experiment is not the result of a heterogeneous spatial distribution of the a and b parameters of the rate-and-state friction model as employed in several simulations of faulting (Barbot et al., 2012). We note that such approaches are based on a continuum description of the interface and do not model the failure of individual asperities where locations in between are contact-free, similar to the inclusion-in-matrix models (e.g., Behr et al., 2021) and the fiber-bundle models (e.g., Daub et al., 2011; Stormo et al., 2016), and hence have zero frictional strength like in our case.

Our results indicate that the slip-strengthening phase, which could be seen as the preparatory phase of large ruptures, includes a population of events that are multi-scale in size (Gutenberg-Richter relation in Figure 13) and in duration (Figure 14). A similar multi-scale size distribution has also been reported for events occurring during the slip-strengthening phase along a sheared fault gouge layer simulated by spherical glass particles that are similar to our asperities (Nasuno et al., 1998). Combined with our results, it implies that this preparatory phase, before a large rupture, is very long with many local events strongly related to the quenched disorder. This result is highly reproducible with the same disorder in the asperity positions.

5.5. Limitations of the Experimental Setup

Our novel experimental setup builds a heterogeneous shear interface of multi-asperity contacts. An important point resulting from the designed configuration is that the elevated adhesion of the silicone block to the asperities is strong enough such that there is no rolling of asperities caused by the shearing imposed on the PMMA plate. Similarly, we also make sure that the silicone block is at no time in contact with the PMMA plate during the experiment. Indeed, in such a case, the high adhesion of the silicone would cause a local resistance to slip and modify the modeled physical process (from friction to adhesion). This limits the maximum normal load we can impose on the system to approximately 1,500 N, at a higher imposed normal load, the silicone block starts to have some local contacts with the PMMA plate.

The sampling rate of the camera employed directly determines the time resolution for tracking the slips of asperities. Thus, the rapid slipping phase involving multiple asperities cannot be analyzed in detail. For example, it is not sampled with a high enough time resolution to capture a clear trend of the decay of the shear force as a function of slip during these episodes (see Figure 9). Furthermore, the precise timing, migration, or interactions of local bead slips during the high slipping phase is not accessible. Finally, as we evidence, the overall rupture during such SEs is slow but it does not preclude that locally during such slow transient, local dynamic rupture occurs such that some proportion of the resolved slip is actually taking place during such dynamic phase and radiate elastic wave. The proportion of the slip taking place on the asperities as dynamic events is presently not measurable but remains to be investigated for future studies. However, we note that such a time-resolution issue also exists when studying natural earthquakes and/or slow slip events. Meanwhile, the velocity threshold defined for each asperity to distinguish IASs and non-IASs is another fundamental parameter that will influence how we treat the temporal slips of asperities, which works the same also for natural geological faults. We argue that increasing the sampling rate would eventually lead to only isolated local slip events. With the current technical setup, the collective SEs clustered with such a relatively low sampling rate are able to reveal some important aspects of the fault physics at scales of both the whole fault and the local asperity.

The derivation of the moment, M_0, of the slip events required the computation of an area, A_i, attached to each asperity (see Equation 8). Here we take for each asperity the area returned by the Voronoi cell including the asperity. Such a definition of the slip area attached to an asperity defines the effective slip area rather than the real slip area during an IAS, which is also commonly seen in natural earthquakes due to the difficulty of determining the discontinuity of slip zones. Indeed, the locked area of an asperity is presumably much lower than a circle of the asperity radius (considering a Hertz contact model) (K. Johnson, 1987). Although some slip deficit can extend beyond the fully locked area, it becomes negligible at a distance typically greater than one asperity radius (L.

Johnson, 2010). It then leads to an overestimation of the computed moment. However, as the contact area for each asperity should be nearly similar (considering again the Hertz contact model and the low stiffness of the silicone) we can expect that the conclusion of the magnitude distribution presented in Figure 13 would be unchanged if one could obtain a precise measurement of the slipping area of each IAS. We thus acknowledge that the reported moment of slip events should be mostly interpreted relatively than as absolute values. Such complexity of the slip distribution is also observed for natural earthquakes with zones of little or no slip (Freymueller et al., 2021).

Another ambiguity is involved in the calculation of the moment from Equation (8). Indeed, the shear modulus used in this equation is taken as the shear modulus of the PMMA. However, the PMMA is the dominant material only on one side of the system, the other side is composed of the PMMA beads embedded in the silicone block. Characterizing the shear modulus for such bi-material is not a trivial task and again further warns against a direct interpretation of the absolute values of M_0.

6. Conclusions

This study analyzes the collective behavior of numerous discrete asperities ($N \approx 140$) modeled on an analog fault interface during multiple seismic cycles. We show that an interface composed of multiple discrete asperities can have a macroscopic behavior that is distinct from that of its individual elements. The asperities present a diversity of slips at various speeds. We evidence the dependency of the interseismic coupling of the interface with the topographical map of the asperity summits and the normal load imposed on the system. We notably show that topographic variations of the asperity summits have a pronounced effect on this coupling. The slip intermittency of the activity of clustered asperities indicates that the interface undergoes local episodes of creep that ultimately lead to the global slip of the interface. The analysis of the evolution of the elastic energy along the interface helps to track the disordering of the asperities with respect to their initial position. We show that this energy is typically higher for large normal stress, which supports the conclusion that normal stress maintains a larger disorder in the system. It shows as well that the disorder increases during the slip-strengthening phase and is only partially reduced during large slip events. Significant statistical features of slip widely observed in natural faults are reproduced by our experiments like the Gutenberg–Richter law, Omori's law, and the moment-duration scaling, suggesting that the obtained results can be extrapolated to natural fault systems.

Data Availability Statement

The experimental data can be available from Shu et al. (2023).

Acknowledgments
We thank Alain Steyer for the technical support. We thank Satoshi Ide, Paul Selvadurai, Mike Heap, and Sylvain Barbot for the discussion. We thank the two anonymous reviewers and the Editor for their helpful comments. This work of the Interdisciplinary Thematic Institute GeoT, as part of the ITI 2021–2028 program of the University of Strasbourg, CNRS and Inserm, was supported by IdEx Unistra (ANR-10-IDEX-0002), and by SFRI-STRAT'US project (ANR ANR-20-SFRI-001) under the framework of the French Investments for the Future Program. This work was also supported by the China Scholarship Council (CSC) Grant 201906370056.

References

Aki, K. (1965). Maximum likelihood estimate of b in the formula log N= a-bM and its confidence limits. *Bulletin of the Earthquake Research Institute, Tokyo University*, *43*, 237–239.

Alava, M. J., Nukala, P. K., & Zapperi, S. (2006). Statistical models of fracture. *Advances in Physics*, *55*(3–4), 349–476. https://doi.org/10.1080/00018730300741518

Albertini, G., Karrer, S., Grigoriu, M. D., & Kammer, D. S. (2021). Stochastic properties of static friction. *Journal of the Mechanics and Physics of Solids*, *147*, 104242. https://doi.org/10.1016/j.jmps.2020.104242

Amitrano, D. (2003). Brittle-ductile transition and associated seismicity: Experimental and numerical studies and relationship with the *b* value. *Journal of Geophysical Research*, *108*(B1). https://doi.org/10.1029/2001jb000680

Ando, R., Nakata, R., & Hori, T. (2010). A slip pulse model with fault heterogeneity for low-frequency earthquakes and tremor along plate interfaces. *Geophysical Research Letters*, *37*(L10310). https://doi.org/10.1029/2010gl043056

Ando, R., Takeda, N., & Yamashita, T. (2012). Propagation dynamics of seismic and aseismic slip governed by fault heterogeneity and Newtonian rheology. *Journal of Geophysical Research*, *117*(B11308). https://doi.org/10.1029/2012jb009532

Ariyoshi, K., Hori, T., Ampuero, J.-P., Kaneda, Y., Matsuzawa, T., Hino, R., & Hasegawa, A. (2009). Influence of interaction between small asperities on various types of slow earthquakes in a 3-D simulation for a subduction plate boundary. *Gondwana Research*, *16*(3–4), 534–544. https://doi.org/10.1016/j.gr.2009.03.006

Aubry, J., Passelègue, F., Escartín, J., Gasc, J., Deldicque, D., & Schubnel, A. (2020). Fault stability across the seismogenic zone. *Journal of Geophysical Research: Solid Earth*, *125*(8), e2020JB019670. https://doi.org/10.1029/2020jb019670

Barbot, S., Lapusta, N., & Avouac, J.-P. (2012). Under the hood of the earthquake machine: Toward predictive modeling of the seismic cycle. *Science*, *336*(6082), 707–710. https://doi.org/10.1126/science.1218796

Baumberger, T., & Caroli, C. (2006). Solid friction from stick–slip down to pinning and aging. *Advances in Physics*, *55*(3–4), 279–348. https://doi.org/10.1080/00018730600732186

Behr, W. M., & Bürgmann, R. (2021). What's down there? The structures, materials and environment of deep-seated slow slip and tremor. *Philosophical Transactions of the Royal Society A*, *379*(2193), 20200218. https://doi.org/10.1098/rsta.2020.0218

Behr, W. M., Gerya, T. V., Cannizzaro, C., & Blass, R. (2021). Transient slow slip characteristics of frictional-viscous subduction megathrust shear zones. *AGU Advances*, *2*(3), e2021AV000416. https://doi.org/10.1029/2021av000416

Ben-David, O., Cohen, G., & Fineberg, J. (2010). The dynamics of the onset of frictional slip. *Science*, *330*(6001), 211–214. https://doi.org/10.1126/science.1194777

Ben-Zion, Y. (2012). Episodic tremor and slip on a frictional interface with critical zero weakening in elastic solid. *Geophysical Journal International*, *189*(2), 1159–1168. https://doi.org/10.1111/j.1365-246x.2012.05422.x

Ben-Zion, Y., & Sammis, C. G. (2003). Characterization of fault zones. *Pure and Applied Geophysics*, *160*(3), 677–715. https://doi.org/10.1007/pl00012554

Bhushan, B. (1998). Contact mechanics of rough surfaces in tribology: Multiple asperity contact. *Tribology Letters*, *4*(1), 1–35. https://doi.org/10.1023/a:1019186601445

Bürgmann, R., Kogan, M. G., Steblov, G. M., Hilley, G., Levin, V. E., & Apel, E. (2005). Interseismic coupling and asperity distribution along the Kamchatka subduction zone. *Journal of Geophysical Research*, *110*(B07405), B07405. https://doi.org/10.1029/2005jb003648

Burridge, R., & Knopoff, L. (1967). Model and theoretical seismicity. *Bulletin of the Seismological Society of America*, *57*(3), 341–371. https://doi.org/10.1785/bssa0570030341

Candela, T., Renard, F., Bouchon, M., Brouste, A., Marsan, D., Schmittbuhl, J., & Voisin, C. (2009). Characterization of fault roughness at various scales: Implications of three-dimensional high resolution topography measurements. *Pure and Applied Geophysics*, *166*(10–11), 1817–1851. https://doi.org/10.1007/s00024-009-0521-2

Candela, T., Renard, F., Klinger, Y., Mair, K., Schmittbuhl, J., & Brodsky, E. E. (2012). Roughness of fault surfaces over nine decades of length scales. *Journal of Geophysical Research*, *117*(B8), B08409. https://doi.org/10.1029/2011jb009041

Carlson, J., & Langer, J. (1989). Mechanical model of an earthquake fault. *Physical Review A*, *40*(11), 6470–6484. https://doi.org/10.1103/physreva.40.6470

Cattania, C., & Segall, P. (2021). Precursory slow slip and foreshocks on rough faults. *Journal of Geophysical Research: Solid Earth*, *126*(4), e2020JB020430. https://doi.org/10.1029/2020jb020430

Chester, F. M., & Chester, J. S. (1998). Ultracataclasite structure and friction processes of the Punchbowl fault, San Andreas system, California. *Tectonophysics*, *295*(1–2), 199–221. https://doi.org/10.1016/s0040-1951(98)00121-8

Chester, F. M., Evans, J. P., & Biegel, R. L. (1993). Internal structure and weakening mechanisms of the San Andreas fault. *Journal of Geophysical Research*, *98*(B1), 771–786. https://doi.org/10.1029/92jb01866

Daub, E. G., Shelly, D. R., Guyer, R. A., & Johnson, P. A. (2011). Brittle and ductile friction and the physics of tectonic tremor. *Geophysical Research Letters*, *38*(10). https://doi.org/10.1029/2011gl046866

Davies, E. R. (2005). *Machine vision: Theory, algorithms, practicalities*. Elsevier.

De Geus, T. W., Popović, M., Ji, W., Rosso, A., & Wyart, M. (2019). How collective asperity detachments nucleate slip at frictional interfaces. *Proceedings of the National Academy of Sciences*, *116*(48), 23977–23983. https://doi.org/10.1073/pnas.1906551116

Dieterich, J. H. (1979). Modeling of rock friction: 1. Experimental results and constitutive equations. *Journal of Geophysical Research*, *84*(B5), 2161–2168. https://doi.org/10.1029/jb084ib05p02161

Dieterich, J. H., & Kilgore, B. D. (1994). Direct observation of frictional contacts: New insights for state-dependent properties. *Pure and Applied Geophysics*, *143*(1), 283–302. https://doi.org/10.1007/bf00874332

Dublanchet, P., Bernard, P., & Favreau, P. (2013). Interactions and triggering in a 3-D rate-and-state asperity model. *Journal of Geophysical Research: Solid Earth*, *118*(5), 2225–2245. https://doi.org/10.1002/jgrb.50187

Faulkner, D., Lewis, A., & Rutter, E. (2003). On the internal structure and mechanics of large strike-slip fault zones: Field observations of the Carboneras fault in southeastern Spain. *Tectonophysics*, *367*(3–4), 235–251. https://doi.org/10.1016/s0040-1951(03)00134-3

Fisher, D. S., Dahmen, K., Ramanathan, S., & Ben-Zion, Y. (1997). Statistics of earthquakes in simple models of heterogeneous faults. *Physical Review Letters*, *78*(25), 4885–4888. https://doi.org/10.1103/physrevlett.78.4885

Fortune, S. (1995). Voronoi diagrams and delaunay triangulations. *Computing in Euclidean Geometry*, 225–265. https://doi.org/10.1142/9789812831699_0007

Frank, W. B. (2016). Slow slip hidden in the noise: The intermittence of tectonic release. *Geophysical Research Letters*, *43*(19), 10–125. https://doi.org/10.1002/2016gl069537

Frank, W. B., & Brodsky, E. E. (2019). Daily measurement of slow slip from low-frequency earthquakes is consistent with ordinary earthquake scaling. *Science Advances*, *5*(10), eaaw9386. https://doi.org/10.1126/sciadv.aaw9386

Freymueller, J. T., Suleimani, E. N., & Nicolsky, D. J. (2021). Constraints on the slip distribution of the 1938 M_W 8.3 Alaska Peninsula earthquake from tsunami modeling. *Geophysical Research Letters*, *48*(9), e2021GL092812. https://doi.org/10.1029/2021gl092812

Gan, G., Ma, C., & Wu, J. (2020). *Data clustering: Theory, algorithms, and applications*. SIAM.

Gao, H., Schmidt, D. A., & Weldon, R. J. (2012). Scaling relationships of source parameters for slow slip events. *Bulletin of the Seismological Society of America*, *102*(1), 352–360. https://doi.org/10.1785/0120110096

Gent, A. N. (1958). On the relation between indentation hardness and Young's modulus. *Rubber Chemistry and Technology*, *31*(4), 896–906. https://doi.org/10.5254/1.3542351

Goebel, T. H., Kwiatek, G., Becker, T. W., Brodsky, E. E., & Dresen, G. (2017). What allows seismic events to grow big? Insights from *b*-value and fault roughness analysis in laboratory stick-slip experiments. *Geology*, *45*(9), 815–818. https://doi.org/10.1130/g39147.1

Gutenberg, B., & Richter, C. F. (1944). Frequency of earthquakes in California. *Bulletin of the Seismological Society of America*, *34*(4), 185–188. https://doi.org/10.1785/bssa0340040185

Gvirtzman, S., & Fineberg, J. (2021). Nucleation fronts ignite the interface rupture that initiates frictional motion. *Nature Physics*, *17*(9), 1037–1042. https://doi.org/10.1038/s41567-021-01299-9

Hanks, T. C., & Kanamori, H. (1979). A moment magnitude scale. *Journal of Geophysical Research*, *84*(B5), 2348–2350. https://doi.org/10.1029/jb084ib05p02348

Harbord, C. W., Nielsen, S. B., De Paola, N., & Holdsworth, R. E. (2017). Earthquake nucleation on rough faults. *Geology*, *45*(10), 931–934. https://doi.org/10.1130/g39181.1

Hyndman, R. D., Yamano, M., & Oleskevich, D. A. (1997). The seismogenic zone of subduction thrust faults. *Island Arc*, *6*(3), 244–260. https://doi.org/10.1111/j.1440-1738.1997.tb00175.x

Ide, S. (2008). A Brownian walk model for slow earthquakes. *Geophysical Research Letters*, *35*(17), L17301. https://doi.org/10.1029/2008gl034821

Ide, S. (2010). Striations, duration, migration and tidal response in deep tremor. *Nature*, *466*(7304), 356–359. https://doi.org/10.1038/nature09251

Ide, S., Beroza, G. C., Shelly, D. R., & Uchide, T. (2007). A scaling law for slow earthquakes. *Nature*, *447*(7140), 76–79. https://doi.org/10.1038/nature05780

Ide, S., & Yabe, S. (2019). Two-dimensional probabilistic cell automaton model for broadband slow earthquakes. *Pure and Applied Geophysics*, *176*(3), 1021–1036. https://doi.org/10.1007/s00024-018-1976-9

Jestin, C., Lengliné, O., & Schmittbuhl, J. (2019). Energy partitioning during subcritical mode i crack propagation through a heterogeneous interface. *Journal of Geophysical Research: Solid Earth*, *124*(1), 837–855. https://doi.org/10.1029/2018jb016831

Johnson, K. (1987). *Contact mechanics*. Cambridge University Press.

Johnson, L. (2010). An earthquake model with interacting asperities. *Geophysical Journal International*, *182*(3), 1339–1373. https://doi.org/10.1111/j.1365-246x.2010.04680.x

Jolivet, R., Candela, T., Lasserre, C., Renard, F., Klinger, Y., & Doin, M.-P. (2015). The burst-like behavior of aseismic slip on a rough fault: The creeping section of the Haiyuan fault, China. *Bulletin of the Seismological Society of America*, *105*(1), 480–488. https://doi.org/10.1785/0120140237

Jolivet, R., Lasserre, C., Doin, M.-P., Peltzer, G., Avouac, J.-P., Sun, J., & Dailu, R. (2013). Spatio-temporal evolution of aseismic slip along the Haiyuan fault, China: Implications for fault frictional properties. *Earth and Planetary Science Letters*, *377*, 23–33. https://doi.org/10.1016/j.epsl.2013.07.020

Kammer, D. S., Radiguet, M., Ampuero, J.-P., & Molinari, J.-F. (2015). Linear elastic fracture mechanics predicts the propagation distance of frictional slip. *Tribology Letters*, *57*(3), 1–10. https://doi.org/10.1007/s11249-014-0451-8

Kanamori, H., & Anderson, D. L. (1975). Theoretical basis of some empirical relations in seismology. *Bulletin of the Seismological Society of America*, *65*(5), 1073–1095.

Khoshmanesh, M., & Shirzaei, M. (2018). Multiscale dynamics of aseismic slip on central San Andreas fault. *Geophysical Research Letters*, *45*(5), 2274–2282. https://doi.org/10.1002/2018gl077017

Kirkpatrick, J. D., Fagereng, Å., & Shelly, D. R. (2021). Geological constraints on the mechanisms of slow earthquakes. *Nature Reviews Earth & Environment*, *2*(4), 285–301. https://doi.org/10.1038/s43017-021-00148-w

Lay, T., & Kanamori, H. (1981). An asperity model of large earthquake sequences. *Earthquake Prediction: International Review*, *4*, 579–592.

Lay, T., Kanamori, H., & Ruff, L. (1982). The asperity model and the nature of large subduction zone earthquakes. *Earthquake Prediction Research*, *1*, 3–71.

Lee, D.-T., & Schachter, B. J. (1980). Two algorithms for constructing a delaunay triangulation. *International Journal of Computer & Information Sciences*, *9*(3), 219–242. https://doi.org/10.1007/bf00977785

Leeman, J., Saffer, D., Scuderi, M., & Marone, C. (2016). Laboratory observations of slow earthquakes and the spectrum of tectonic fault slip modes. *Nature Communications*, *7*(1), 1–6. https://doi.org/10.1038/ncomms11104

Lengliné, O., Elkhoury, J., Daniel, G., Schmittbuhl, J., Toussaint, R., Ampuero, J.-P., & Bouchon, M. (2012). Interplay of seismic and aseismic deformations during earthquake swarms: An experimental approach. *Earth and Planetary Science Letters*, *331*, 215–223. https://doi.org/10.1016/j.epsl.2012.03.022

Lengliné, O., Frank, W. B., Marsan, D., & Ampuero, J.-P. (2017). Imbricated slip rate processes during slow slip transients imaged by low-frequency earthquakes. *Earth and Planetary Science Letters*, *476*, 122–131. https://doi.org/10.1016/j.epsl.2017.07.032

Li, T., & Rubin, A. M. (2017). A microscopic model of rate and state friction evolution. *Journal of Geophysical Research: Solid Earth*, *122*(8), 6431–6453. https://doi.org/10.1002/2017jb013970

Luo, Y., & Ampuero, J.-P. (2018). Stability of faults with heterogeneous friction properties and effective normal stress. *Tectonophysics*, *733*, 257–272. https://doi.org/10.1016/j.tecto.2017.11.006

Marone, C. (1998). Laboratory-derived friction laws and their application to seismic faulting. *Annual Review of Earth and Planetary Sciences*, *26*(1), 643–696. https://doi.org/10.1146/annurev.earth.26.1.643

McLaskey, G. C., & Glaser, S. D. (2011). Micromechanics of asperity rupture during laboratory stick slip experiments. *Geophysical Research Letters*, *38*(12), L12302. https://doi.org/10.1029/2011gl047507

McLaskey, G. C., Thomas, A. M., Glaser, S. D., & Nadeau, R. M. (2012). Fault healing promotes high-frequency earthquakes in laboratory experiments and on natural faults. *Nature*, *491*(7422), 101–104. https://doi.org/10.1038/nature11512

Mitchell, T., & Faulkner, D. (2009). The nature and origin of off-fault damage surrounding strike-slip fault zones with a wide range of displacements: A field study from the Atacama fault system, northern Chile. *Journal of Structural Geology*, *31*(8), 802–816. https://doi.org/10.1016/j.jsg.2009.05.002

Morad, D., Sagy, A., Tal, Y., & Hatzor, Y. H. (2022). Fault roughness controls sliding instability. *Earth and Planetary Science Letters*, *579*, 117365. https://doi.org/10.1016/j.epsl.2022.117365

Moreno, M. S., Bolte, J., Klotz, J., & Melnick, D. (2009). Impact of megathrust geometry on inversion of coseismic slip from geodetic data: Application to the 1960 Chile earthquake. *Geophysical Research Letters*, *36*(L16310), L16310. https://doi.org/10.1029/2009gl039276

Nadeau, R. M., & Johnson, L. R. (1998). Seismological studies at Parkfield VI: Moment release rates and estimates of source parameters for small repeating earthquakes. *Bulletin of the Seismological Society of America*, *88*(3), 790–814. https://doi.org/10.1785/bssa0880030790

Nakata, R., Ando, R., Hori, T., & Ide, S. (2011). Generation mechanism of slow earthquakes: Numerical analysis based on a dynamic model with brittle-ductile mixed fault heterogeneity. *Journal of Geophysical Research*, *116*(B08308), B08308. https://doi.org/10.1029/2010jb008188

Nasuno, S., Kudrolli, A., Bak, A., & Gollub, J. P. (1998). Time-resolved studies of stick-slip friction in sheared granular layers. *Physical Review E*, *58*(2), 2161–2171. https://doi.org/10.1103/physreve.58.2161

Perfettini, H., Avouac, J.-P., Tavera, H., Kositsky, A., Nocquet, J.-M., Bondoux, F., et al. (2010). Seismic and aseismic slip on the Central Peru megathrust. *Nature*, *465*(7294), 78–81. https://doi.org/10.1038/nature09062

Perfettini, H., Schmittbuhl, J., & Vilotte, J.-P. (2001). Slip correlations on a creeping fault. *Geophysical Research Letters*, *28*(10), 2137–2140. https://doi.org/10.1029/2000gl012343

Pohrt, R., & Popov, V. L. (2012). Normal contact stiffness of elastic solids with fractal rough surfaces. *Physical Review Letters*, *108*(10), 104301. https://doi.org/10.1103/physrevlett.108.104301

Power, W., Tullis, T., Brown, S., Boitnott, G., & Scholz, C. (1987). Roughness of natural fault surfaces. *Geophysical Research Letters*, *14*(1), 29–32. https://doi.org/10.1029/gl014i001p00029

Rivière, J., Lv, Z., Johnson, P., & Marone, C. (2018). Evolution of *b*-value during the seismic cycle: Insights from laboratory experiments on simulated faults. *Earth and Planetary Science Letters*, *482*, 407–413. https://doi.org/10.1016/j.epsl.2017.11.036

Romanet, P., Bhat, H. S., Jolivet, R., & Madariaga, R. (2018). Fast and slow slip events emerge due to fault geometrical complexity. *Geophysical Research Letters*, *45*(10), 4809–4819. https://doi.org/10.1029/2018gl077579

Rousset, B., Jolivet, R., Simons, M., Lasserre, C., Riel, B., Milillo, P., et al. (2016). An aseismic slip transient on the north Anatolian fault. *Geophysical Research Letters*, *43*(7), 3254–3262. https://doi.org/10.1002/2016gl068250

Ruff, L., & Kanamori, H. (1983). The rupture process and asperity distribution of three great earthquakes from long-period diffracted P-waves. *Physics of the Earth and Planetary Interiors*, *31*(3), 202–230. https://doi.org/10.1016/0031-9201(83)90099-7

Ruina, A. (1983). Slip instability and state variable friction laws. *Journal of Geophysical Research*, *88*(B12), 10359–10370. https://doi.org/10.1029/jb088ib12p10359

Schmittbuhl, J., Chambon, G., Hansen, A., & Bouchon, M. (2006). Are stress distributions along faults the signature of asperity squeeze? *Geophysical Research Letters*, *33*(13), L13307. https://doi.org/10.1029/2006gl025952

Schmittbuhl, J., Gentier, S., & Roux, S. (1993). Field measurements of the roughness of fault surfaces. *Geophysical Research Letters*, *20*(8), 639–641. https://doi.org/10.1029/93gl00170

Schmittbuhl, J., & Måløy, K. J. (1997). Direct observation of a self-affine crack propagation. *Physical Review Letters*, *78*(20), 3888–3891. https://doi.org/10.1103/physrevlett.78.3888

Schmittbuhl, J., Schmitt, F., & Scholz, C. (1995). Scaling invariance of crack surfaces. *Journal of Geophysical Research*, *100*(B4), 5953–5973. https://doi.org/10.1029/94jb02885

Schmittbuhl, J., Vilotte, J.-P., & Roux, S. (1996). A dissipation-based analysis of an earthquake fault model. *Journal of Geophysical Research*, *101*(B12), 27741–27764. https://doi.org/10.1029/96jb02294

Scholz, C. (2015). On the stress dependence of the earthquake *b* value. *Geophysical Research Letters*, *42*(5), 1399–1402. https://doi.org/10.1002/2014gl062863

Scholz, C. (2019). *The mechanics of earthquakes and faulting*. Cambridge University Press.

Scholz, C., & Campos, J. (1995). On the mechanism of seismic decoupling and back arc spreading at subduction zones. *Journal of Geophysical Research*, *100*(B11), 22103–22115. https://doi.org/10.1029/95jb01869

Scholz, C., & Campos, J. (2012). The seismic coupling of subduction zones revisited. *Journal of Geophysical Research*, *117*(B05310). https://doi.org/10.1029/2011jb009003

Schulz, S. E., & Evans, J. P. (2000). Mesoscopic structure of the Punchbowl Fault, Southern California and the geologic and geophysical structure of active strike-slip faults. *Journal of Structural Geology*, *22*(7), 913–930. https://doi.org/10.1016/s0191-8141(00)00019-5

Selvadurai, P. A., & Glaser, S. D. (2015). Laboratory-developed contact models controlling instability on frictional faults. *Journal of Geophysical Research: Solid Earth*, *120*(6), 4208–4236. https://doi.org/10.1002/2014jb011690

Selvadurai, P. A., & Glaser, S. D. (2017). Asperity generation and its relationship to seismicity on a planar fault: A laboratory simulation. *Geophysical Journal International*, *208*(2), 1009–1025. https://doi.org/10.1093/gji/ggw439

Shu, W., Lengliné, O., & Schmittbuhl, J. (2023). Experimental dataset of collective behavior of asperities before large stick-slip events [Dataset]. CDGP Data. https://doi.org/10.25577/2023-SHU-JGR

Stierman, D. J. (1984). Geophysical and geological evidence for fracturing, water circulation and chemical alteration in granitic rocks adjacent to major strike-slip faults. *Journal of Geophysical Research*, *89*(B7), 5849–5857. https://doi.org/10.1029/jb089ib07p05849

Stormo, A., Lengliné, O., Schmittbuhl, J., & Hansen, A. (2016). Soft-clamp fiber bundle model and interfacial crack propagation: Comparison using a non-linear imposed displacement. *Frontiers in Physics*, *4*, 18. https://doi.org/10.3389/fphy.2016.00018

Subarya, C., Chlieh, M., Prawirodirdjo, L., Avouac, J.-P., Bock, Y., Sieh, K., et al. (2006). Plate-boundary deformation associated with the great Sumatra–Andaman earthquake. *Nature*, *440*(7080), 46–51. https://doi.org/10.1038/nature04522

Sutton, M. A., Orteu, J. J., & Schreier, H. (2009). *Image correlation for shape, motion and deformation measurements: Basic concepts, theory and applications*. Springer Science & Business Media.

Tanguy, A., Gounelle, M., & Roux, S. (1998). From individual to collective pinning: Effect of long-range elastic interactions. *Physical Review E*, *58*(2), 1577–1590. https://doi.org/10.1103/physreve.58.1577

Utsu, T., Ogata, Y., & Matsu'ura, R. (1995). The centenary of the Omori formula for a decay law of aftershock activity. *Journal of Physics of the Earth*, *43*(1), 1–33. https://doi.org/10.4294/jpe1952.43.1

Wech, A. G., Creager, K. C., Houston, H., & Vidale, J. E. (2010). An earthquake-like magnitude-frequency distribution of slow slip in northern Cascadia. *Geophysical Research Letters*, *37*(L22310). https://doi.org/10.1029/2010gl044881

Wu, B. S., & McLaskey, G. C. (2019). Contained laboratory earthquakes ranging from slow to fast. *Journal of Geophysical Research: Solid Earth*, *124*(10), 10270–10291. https://doi.org/10.1029/2019jb017865

Xu, S., Fukuyama, E., Yamashita, F., Kawakata, H., Mizoguchi, K., & Takizawa, S. (2023). Fault strength and rupture process controlled by fault surface topography. *Nature Geoscience*, *16*, 1–7. https://doi.org/10.1038/s41561-022-01093-z

Yamashita, F., Fukuyama, E., Xu, S., Kawakata, H., Mizoguchi, K., & Takizawa, S. (2021). Two end-member earthquake preparations illuminated by foreshock activity on a meter-scale laboratory fault. *Nature Communications*, *12*(1), 1–11. https://doi.org/10.1038/s41467-021-24625-4

Yuen, H., Princen, J., Illingworth, J., & Kittler, J. (1990). Comparative study of Hough transform methods for circle finding. *Image and Vision Computing*, *8*(1), 71–77. https://doi.org/10.1016/0262-8856(90)90059-e